ANALYTICAL AND EXPERIMENTAL STUDY
OF LIQUID-ULLAGE COUPLING AND LOW GRAVITY
INTERFACE STABILITY

Prepared for

NATIONAL AERONAUTICS AND SPACE ADMINISTRATION

GEORGE C. MARSHALL SPACE FLIGHT CENTER

Huntsville, Alabama

Lockheed
MISSILES & SPACE COMPANY
A GROUP DIVISION OF LOCKHEED AIRCRAFT CORPORATION

SUNNYVALE, CALIFORNIA

ANALYTICAL AND EXPERIMENTAL STUDY OF LIQUID-ULLAGE COUPLING AND LOW GRAVITY INTERFACE STABILITY

Contributors

S. E. Hurd

M. P. Hollister

J. H. Chin

H. M. Satterlee

E. Y. Harper

Approved: _____
F. L. Hines, Study Leader
Launch and Entry Thermodynamics

Approved: _____
A. M. Levy, Manager
Launch and Entry Thermodynamics

Lockheed

M I S S I L E S & S P A C E C O M P A N Y

A GROUP DIVISION OF LOCKHEED AIRCRAFT CORPORATION

SUNNYVALE, CALIFORNIA

FOREWORD

This report was prepared by Launch and Entry Thermodynamics of the Flight Technology— Engineering organization, Research and Development Division, Lockheed Missiles & Space Company, for the George C. Marshall Space Flight Center (MSFC) of the National Aeronautics and Space Administration (NASA).

The report summarizes the principal results obtained during the period from 1 June 1965 through 29 August 1966, which constitutes the third and final phase of the contract. This summary report and those documenting the first and second phases of the study comprise the contract final report.

LOCKHEED MISSILES & SPACE COMPANY

CONTENTS

LOCKHEED MISSILES & SPACE COMPANY

LOCKHEED MISSILES & SPACE COMPANY

ILLUSTRATIONS

TABLES

LOCKHEED MISSILES & SPACE COMPANY

NOMENCLATURE

A	area, ft^2
b	slit width, cm
Bo	Bond number, $g R^2 \rho / \sigma$
c_p	specific heat at constant pressure, Btu/lb_m -° F
c_v	specific heat at constant volume, Btu/lb_m -° F
D	diffusion coefficient, ft^2/sec
f	enthalpy function defined in Eq. (2.4), Btu/lb_m
F	enthalpy function defined in Eq. (2.5), Btu/lb_m , also, liquid height above datum at $r = 0$
Fr	Froude number, u^2/gR
g	local acceleration, ft/sec^2 (or cm/sec^2)
Gr_H^*	modified Grashof number for liquids, $g q_w \beta H^4 / k_L \nu_L^2$
Gr_R^*	modified Grashof number for vapor, $g \beta_v q_u R^4 / k_v \nu_v^2$
Gr_R	Grashof number for vapor, $g \beta_v (T_{u\,htr} - T_u) R^3 / \nu_v^2$
h^*	specific enthalpy, Btu/lb_m
h	heat transfer coefficient, Btu/ft^2-sec-° F
H	effective height of heated liquid sidewall, ft, also, integration step size
H'	effective total height of liquid, ft
I	energy integral defined in Eq. (2.19)
J	mechanical equivalent of heat, 778 ft-lb_f/Btu
k	thermal conductivity, Btu/ft-sec-° F
ℓ	liquid height above stable interface
L	effective height of heated ullage sidewall, ft
L'	effective total height of ullage, ft
m	mass, lb_m
$\dot{m}$	mass transfer rate, lb_m/sec

$\dot{m}'$	mass transfer rate, per unit interface area, lb_m/ft^2-sec
n	exponent in Eq. (2.24)
Nu	Nusselt number, hR/k
p	pressure, lb_f/ft^2
Pr	Prandtl number, $\mu c_p/k$
q	heat flux, Btu/ft^2-sec
q_L	heat flux to interface from liquid film
q_u	heat flux to ullage
q_v	heat flux to vapor film from interface
r	radial distance normalized by tank radius
R	tank radius, ft
Ra*	modified Rayleigh number, $Gr_H^* Pr$
$\mathcal{R}$	gas constant, Btu/lb_m-°R
t	time, sec
T	temperature, °R or °F
u	velocity, ft/sec or cm/sec
u_m	maximum boundary layer or jet velocity, cm/sec
u_s	maximum surface radial velocity, cm/sec
u*	slip velocity in boiling boundary layer, u_v/u_L
U	normalized surface velocity, u/u_m (denoted as V in program language)
v	specific volume, ft^3/lb_m
V	volume, ft^3
w	vapor concentration
We	Weber number, $u^2 R\rho/\sigma$
x	boundary layer run length
y	coordinate normal to wall, ft
z	distance from liquid surface, ft
Z	compressibility factor
$\bar{\alpha}$	mean vapor fraction in boiling boundary layer
β	coefficient of thermal expansion, °R^{-1}
δ	film thickness, ft, or jet thickness, cm
Δ	height (depth) of stratified layer, ft
Δ'	stratified layer thickness with no bottom heating, ft

ϵ	tank longitudinal strain coefficient, $\mathrm{ft}^2/\mathrm{lb}_f$
ζ	defined in Eq. (3.4)
θ	liquid-wall contact angle
λ	latent heat of vaporization, $\mathrm{Btu}/\mathrm{lb}_m$
μ	dynamic viscosity, $\mathrm{lb}_m/\mathrm{ft\text{-}sec}$
ν	kinematic viscosity, $\mathrm{ft}^2/\mathrm{sec}$
ρ	density, $\mathrm{lb}_m/\mathrm{ft}^3$ or $\mathrm{g}_m/\mathrm{cm}^3$
$\rho*$	density ratio in boiling boundary layer, ρ_v/ρ_L
σ	surface tension, dyne/cm
τ	capillary response time, sec
ψ	mass transfer factor, defined in Eqs. (2.12) and (2.15)

Subscripts

a	ambient (external to tank)
av	average
b	boiling
B	bottom
BL	boundary layer
f	interface or saturation
L	liquid or limiting value
o	initial or reference quantity
p	constant pressure or pressurant
s	liquid surface
t	total
T	constant temperature
TR	transitional
u	ullage
uhtr	ullage heater
v	vapor
w	heated liquid sidewall
1	local condition

Section 1
INTRODUCTION AND SUMMARY

Liquid-ullage coupling may be broadly described as the thermodynamic interaction between the liquid and vapor phases of a contained fluid system. This phenomenon is influenced by the energy transport modes in each of the fluid phases, and is a controlling factor in the self-pressurization of a closed, heated container. Stratification is defined as the development of temperature gradients in a contained fluid. Stratification can be caused by a free-convection boundary layer on the wall which carries heated fluid to the top of the container, forming a growing layer of liquid which is at a higher temperature than the bulk of the liquid. Of particular interest is the relation between liquid stratification and the energy transfer at the liquid-vapor interface.

These phenomena are of particular importance in cryogenic propellant tanks and can have a significant effect on vehicle design and operation. The design of venting devices, pressurization systems, insulation methods, propellant feed pumps, and tank structures may be substantially influenced by these phenomena.

An additional problem associated with large cryogenic propellant tanks is that of "boundary layer breakthrough"; i.e., the momentum existing in the free-convection boundary layer can cause instability of the liquid-ullage interface at the time of engine shutdown. To ensure reliable designs, and to avoid excessive penalties due to conservatism in prediction methods, sound analytical models and experimental data applicable to the conditions of interest are required.

This document presents the results of the analytical and experimental work carried out by the Lockheed Missiles & Space Company (LMSC) for the NASA-George C. Marshall Space Flight Center (MSFC) on the problems of liquid-ullage coupling and boundary layer breakthrough, under Phase III of the contract, entitled "Theoretical and Experimental Studies of Zero-G Heat Transfer Modes." The work reported was conducted

LOCKHEED MISSILES & SPACE COMPANY

over a 14-month period, from 1 June 1965 through 31 July 1966. The results of Phases I and II of the Study were reported in Refs. 1 and 2, respectively.

The major objective of the study has been to perform theoretical analyses of the heat transfer phenomena occurring in cryogenic liquids and to derive an analytical model for predicting temperature stratification and ullage pressure in cryogenic tanks. Auxiliary objectives have been to conduct stratification and liquid-ullage coupling experiments in noncryogenic fluids to demonstrate the validity of scaling laws for stratification and to check the analytical models developed, and to perform drop-tower experiments to confirm the criteria derived to define the boundary layer breakthrough problem.

The highlights of Phase III of the study are summarized in this Section.

1.1 LIQUID-ULLAGE COUPLING ANALYSIS

A mathematical model and corresponding analysis which describe liquid-ullage coupling have been developed in Phase II of this study. In Phase III, a similar but more extensive model has been formulated which includes arbitrary pressurization with a noncondensible gas, bottom heating, and nucleate boiling in the boundary layer. In addition, the model considers transition from laminar to turbulent flow in the free-convection boundary layer, tank volume change due to tank strain, and arbitrary end geometry for a cylindrical tank. The results of the analysis are expressed in terms of a system of equations which can be solved simultaneously to give the ullage pressure and temperature, intefacial mass transfer, the liquid surface and bulk temperatures, and the liquid level, as functions of time. A FORTRAN computer program which solves this system of equations has been written.

1.2 LIQUID-ULLAGE COUPLING EXPERIMENTS

The liquid-ullage coupling models which have been developed contain three parameters which must be experimentally determined: the vapor-side interface heat-transfer coefficient, h_V, the liquid-side interface heat-transfer coefficient, h_L, and the

liquid energy integral I. An experimental program has been conducted to establish the validity of the mathematical models and to develop empirical correlations for the three required parameters. Experiments have been conducted over a range of ullage and liquid heat fluxes using water and Freon 11 as the working fluids. Tests also have been conducted with nucleate boiling in the boundary layer and with controlled ullage venting.

Predictions from the simpler liquid-ullage coupling model were compared with the experimental data to determine those values for h_v, h_L, and I which result in the best agreement between the model and the data. This was also done for the applicable hydrogen data (obtained from MSFC tests in a full-scale S-IV tank). The resulting values for the liquid Nusselt number were correlated as a function of the liquid modified Grashof number, and the vapor Nusselt number was correlated with vapor modified Grashof number. A preliminary correlation of the energy integral was obtained using the liquid modified Grashof number and a dimensionless form of the latent heat of vaporization.

In general, predictions obtained from the model using the appropriate values for h_v, h_L, and I agreed well with the data. This was true for runs both with and without boiling in the liquid boundary layer and for runs with controlled ullage venting.

1.3 INTERFACE STABILITY ANALYSIS

In Phase I of the study, the influence of surface velocities on the shape of the meniscus was studied analytically through numerical solutions of the governing differential equation. The numerical integration scheme has been modified to determine, by an iteration technique, the limiting Weber number above which solutions cannot be obtained within the numerical model used. The results of this modified program indicate that the surface velocity distribution has a significant effect on the calculated limiting Weber number.

1.4 INTERFACE STABILITY EXPERIMENTS

Experiments were performed to obtain data on the effect on free surface stability of convective flow patterns in a liquid under reduced gravity conditions. A pump-operated recirculating flow tank was used to generate a range of flow conditions qualitatively simulating the free-convection boundary layer and associated free surface flow in a partially-full cryogenic propellant tank. Tests at standard gravity were employed to study the free surface velocity distribution, and drop-tower tests at zero and reduced gravity exhibited the effect of these flow patterns on interface stability.

From motion pictures taken during the drop-tower experiments, it was observed that free surface Weber numbers greater than 50 resulted in an unstable interface when the gravity level was reduced to zero. The stabilizing effect of a finite acceleration was evident, and very little distortion of the free-surface shape occurred at a Froude number of 0.2.

Section 2

LIQUID-ULLAGE COUPLING

When a closed container which is partially filled with a saturated liquid is heated, mass and energy transfer will occur at the liquid-vapor interface, and the pressure and temperature within the container will change. The complicated physical phenomena which occur in such a container are referred to as "liquid-ullage coupling." A mathematical model and corresponding analysis which describe liquid-ullage coupling were developed and presented in Ref. 2. During the present reporting period, this model was modified to extend the range of application. This section compares this modified model with data obtained from a series of liquid-ullage coupling tests. In addition, a new liquid-ullage coupling model, similar to, but more extensive than, that of Ref. 2, will be presented.

2.1 ANALYSIS

This subsection describes both the modifications to the original liquid-ullage coupling model, with which the experimental data are compared, and the new model which considers a two-component ullage and nonperfect fluids.

2.1.1 Extension of Original Model

The liquid-ullage coupling model developed during Phase II of this study (Ref. 2) has been extended to consider:

- Mass addition of the fluid vapor at an arbitrary temperature
- The effect of nucleate boiling in the boundary layer on the rate of liquid stratification

LOCKHEED MISSILES & SPACE COMPANY

For the first change, the ullage energy balance equation (Eq. 5.4 of Ref. 2) was modified to include an arbitrary pressurant inlet temperature $T_p(t)$:

$$\left(\frac{2L}{R}\right)q_u + q_v + \dot{m}_f' c_{p_v} T_f + \dot{m}_p' c_{p_v} T_p = \frac{d\left(m_v c_{v_v} T_u\right)}{dt} + \frac{p}{J}\frac{dL}{dt} \qquad (2.1)$$

The consideration of nucleate boiling in the boundary layer is restricted to the hydrodynamic effect of increasing the boundary layer heat transfer coefficient and mass flow. The effect of vapor bubbles that do not condense before reaching the liquid surface, thereby directly affecting the rate of pressurization, is not considered. Using the boiling boundary layer analysis of Ref. 2, and assuming a uniform vapor distribution, yields the following expression for the rate of growth of the stratified layer:

$$\left(\frac{d\Delta}{dt}\right)_b = \frac{\dfrac{8xh_b}{R\rho_L c_{p_L}}}{\left(\dfrac{\rho^* u^* \overline{\alpha}}{1-\overline{\alpha}}\right)\left(\dfrac{4\lambda h_b}{q_w c_{p_L}}\right) + 1} \qquad (2.2)$$

Transition from a boiling to a nonboiling boundary-layer mass flow rate is accommodated by assuming a linear variation between specified values of wall superheat which represent the nonboiling and fully developed boiling criteria.

2.1.2 New Liquid-Ullage Coupling Model

The new liquid-ullage coupling model and the nomenclature used in the analysis are presented in Fig. 2-1. The analysis is based on the following assumptions:

- The convection current in the ullage is strong enough so that the bulk of the ullage is at a uniform temperature and species concentration.
- Temperature and concentration gradients in the ullage exist only across a film of negligible mass adjacent to the liquid-ullage interface.
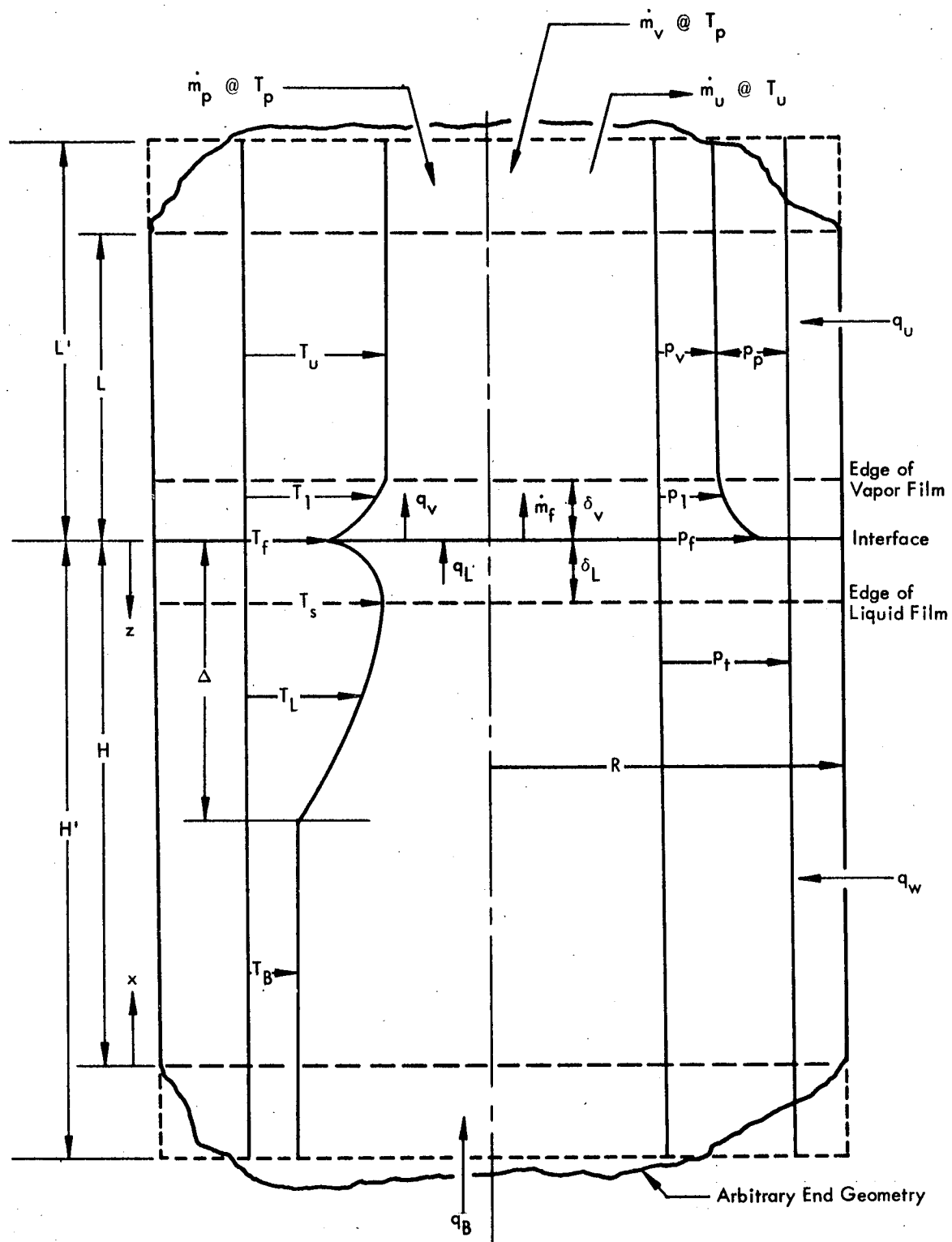
Fig. 2-1 System Model Used in Liquid-Ullage Coupling Analysis

- The vapor and pressurant are characterized by a modified perfect gas law.
- The specific heats of the ullage vapor and pressurant are constant with respect to temperature.
- The partial pressure of the vapor at the interface is the saturation pressure corresponding to the liquid-vapor interface temperature.
- The properties of the liquid (except the density in considering bouyant flow) are constant.
- The interface area is constant.

Additional features not considered in the original analysis include:

- Arbitrary pressurization with a noncondensible gas
- A more complete consideration of the effects of bottom heating
- Transition from laminar to turbulent free-convection boundary layer
- Tank volume change due to tank strain
- Cylindrical tank with arbitrary end geometry

It is assumed that the tank can be represented by an "equivalent cylinder" such that the interface area and the change in liquid and ullage volumes with interface position are constant. The distance below the liquid surface at which the free convection boundary layer begins is defined as H. The distance L is defined so that the ullage heated wall area is $2\pi RL$. H' and L' define the liquid and ullage volumes:

$$V_L = \pi R^2 H' \quad \text{and} \quad V_u = \pi R^2 L'$$

The bottom heat flux is adjusted so that the correct total bottom heat rate is expressed by $\pi R^2 q_B$.

An energy balance on the ullage gives

$$(q_u A_u + q_v A_s)\, dt + \dot{m}_f \left\{ \left(c_{p_v} \right)_{p_f} (T_f - T_o) - \left[F_v(p_f) - F_v(p_v) \right] \right\} dt$$

$$+ \dot{m}_v \left\{ \left(c_{p_v} \right)_{p_t} (T_p - T_o) - \left[F_v(p_t) - F_v(p_v) \right] \right\} dt$$

$$+ \dot{m}_p \left\{ \left(c_{p_p} \right)_{p_t} (T_p - T_o) - \left[F_p(p_t) - F_p(p_p) \right] \right\} dt$$

$$- w \dot{m}_u \left(c_{p_v} \right)_{p_v} (T_u - T_o)\, dt - (1 - w) \dot{m}_u \left(c_{p_p} \right)_{p_p} (T_u - T_o)\, dt$$

$$= \left(c_{p_v} \right)_{p_v} d\left[m_v (T_u - T_o) \right] + \left(c_{p_p} \right)_{p_p} d\left[m_p (T_u - T_o) \right]$$

$$+ \left\{ m_v \left[f_v(p_v) + (T_u - T_o) \left(\frac{dc_{p_v}}{dp} \right) \right] - \frac{V_u}{J} \right\} dp_v$$

$$+ \left\{ m_p \left[f_p(p_p) + (T_u - T_o) \left(\frac{dc_{p_p}}{dp} \right) \right] - \frac{V_u}{J} \right\} dp_p \qquad (2.3)$$

where

$$f_v(p) = \left(\frac{\partial h_v^*}{\partial p}\right)_{T_o} \tag{2.4}$$

and

$$F_v(p) = \int_{p_o}^{p} f_v(p)\, dp \tag{2.5}$$

These expressions are derived in Ref. 3, where the energy datum is taken as the specific enthalpy of the liquid at an arbitrary saturated-liquid reference state defined by T_o and p_o.

Equation (2.3) includes the following assumptions:

- The entering gas streams, $\dot{m}_v$ and $\dot{m}_p$, enter at the system total pressure, p_t.
- The vapor entering due to vaporization of the liquid, $\dot{m}_f$, enters the system at the vapor pressure, p_f, corresponding to the interface temperature, T_f.
- The vented mass, $\dot{m}_u$, leaves at the same vapor concentration, w, as the mixed ullage.

An energy balance on the entire liquid system yields

$$\left[q_w A_w + q_B A_B - q_L A_s - \dot{m}_f c_{p_L}\left(T_f - T_o\right)\right] dt$$

$$= c_{p_L} d\left[\int_0^\Delta \rho_L\left(T_L - T_o\right)(dV/dz)dz\right] + c_{p_L} d\left[\rho_B\left(T_B - T_o\right)V_B\right]$$

$$- \left(\beta T_o V_L/J\right) dp_t \tag{2.6}$$

Assuming that all bottom heating energy remains in the bulk liquid, an energy balance on the bulk liquid gives

$$q_B A_B \, dt = c_{p_L} \, d \left[\rho_B \left(T_B - T_o \right) V_B \right] - \left(\beta T_o V_B / J \right) dp_t \qquad (2.7)$$

To determine surface temperature, an additional energy balance is required. Since it is assumed that the surface temperature is unaffected by bottom heating, an energy balance may be made on the liquid system assuming no bottom heating. This gives

$$\left[q_w A_w - q_L A_s - \dot{m}_f c_{p_L} \left(T_f - T_o \right) \right] dt$$

$$= c_{p_L} \, d \left[\int_0^{\Delta'} \rho_L \left(T_L - T_o \right) (dV/dz) \, dz \right] - \left(\beta T_o V_L / J \right) dp_t \qquad (2.8)$$

where Δ' is the stratified layer depth with no bottom heating. Reference 1 gives expressions for Δ' for laminar and turbulent free convection boundary layers, and Eq. (2.2) provides an alternate expression to be used when boiling exists in the boundary layer. Transition from a nonboiling to a boiling boundary layer is accomplished as described in Section 2.1.1.

An energy balance on the liquid-vapor interface yields

$$(q_L - q_v) A_s = \dot{m}_f \lambda \qquad (2.9)$$

Liquid and vapor interfacial heat transfer coefficients are defined such that

$$q_L = h_L (T_s - T_f) \psi_L \qquad (2.10)$$

where

$$h_L = k_L/\delta_L \tag{2.11}$$

$$\psi_L = \frac{c_{p_L} \dot{m}_f/h_L A_s}{1 - \exp\left(- c_{p_L} \dot{m}_f/h_L A_s\right)} \tag{2.12}$$

and

$$q_v = h_v (T_u - T_f) \psi_v \tag{2.13}$$

where

$$h_v = k_v/\delta_v \tag{2.14}$$

$$\psi_v = \frac{c_{p_v} \dot{m}_f/h_v A_s}{1 - \exp\left(c_{p_v} \dot{m}_f/h_v A_s\right)} \tag{2.15}$$

Equations (2.12) and 2.15) result from integration of the rate equations for the liquid and vapor films, using a quasi steady-state approximation and the assumption that the films have negligible mass and thermal capacity. This approach is the same as that used in the earlier analysis of Ref. 2; details of the method are presented in Refs. 3 and 4.

A mass balance on each of the species in the ullage yields

$$\frac{dm_v}{dt} = \dot{m}_v + \dot{m}_f - w\dot{m}_u \tag{2.16}$$

and

$$\frac{dm_p}{dt} = \dot{m}_p - (1 - w)\dot{m}_u \tag{2.17}$$

A mass balance on the liquid gives, approximately (Ref. 3),

$$\dot{m}_f = A_s \beta \rho_o \frac{d}{dt} \int_0^{H'} \left(T_L - T_o\right) dz - \rho_o A_s \frac{dH'}{dt} \tag{2.18}$$

Following the approach used to obtain the closed-form, integral technique stratification solutions of Refs. 1 and 2, an energy integral is specified for the stratified layer as

$$I = \int_0^1 \left(\frac{T_L - T_B}{T_S - T_B}\right) d\left(\frac{z}{\Delta}\right) \tag{2.19}$$

The state equations for each of the species in the ullage are

$$p_v V_u = m_v Z_v \mathcal{R}_v T_u J \tag{2.20}$$

$$p_p V_u = m_p Z_p \mathcal{R}_p T_u J \tag{2.21}$$

Dalton's Law for mixtures of nonreacting gases relates the species partial pressures to the system total pressure:

$$\frac{dp_v}{dt} + \frac{dp_p}{dt} = \frac{dp_t}{dt} \tag{2.22}$$

Also, the Clapeyron relation is used to relate T_f and p_f:

$$\ln \left(\frac{p_f}{p_o}\right) \cong \left(\frac{\lambda}{Z_f}\right)_o \frac{1}{\mathcal{R}_v} \left(\frac{1}{T_o} - \frac{1}{T_f}\right) \qquad (2.23)$$

When a noncondensible pressurant is used, Stefan's diffusion law is integrated across the vapor film from $z = 0$ to $z = -\delta_v$ assuming

$$\frac{T_u - T_1}{T_u - T_f} = \left(1 + \frac{z}{\delta_v}\right)^n \qquad (2.24)$$

to yield

$$\dot{m}_f = \frac{D p_t (n + 1) A_s}{J \mathcal{R}_v Z_v \delta_v (n T_u + T_f)} \ln \left(\frac{p_t - p_v}{p_t - p_f}\right) \qquad (2.25)$$

Finally, if the tank is allowed to expand with increased gage pressure,

$$V_u + V_L = V_{t_o} \left\{ 1 + \epsilon \left[\left(p_t - p_a\right) - \left(p_t - p_a\right)_o \right] \right\} \qquad (2.26)$$

The above system of equations can be solved to give the ullage pressure and temperature, the interfacial mass transfer, the liquid surface and bulk temperatures, and the liquid level as functions of time. A FORTRAN computer program has been written which solves this system of equations integrating the differential equations by a forward finite-difference technique.

2.2 EXPERIMENTS

The liquid-ullage coupling models which have been developed contain three parameters which must be experimentally determined: h_v, h_L, and I. An experimental program was conducted to establish the validity of the ullage coupling model and to develop empirical, dimensionless correlations for the three required parameters. The approach used was to establish values for h_v, h_L, and I which most accurately predicted the experimental pressure, ullage temperature, and interfacial mass transfer for each run. This work is an extension of that begun during Phase II of the study, in which only limited liquid-ullage coupling data were obtained.

2.2.1 Facility and Experimental Procedures

The pressure vessel facility described in Ref. 2 was modified so that it could be used for the liquid-ullage coupling experiments. A schematic of the apparatus and associated plumbing is shown in Fig. 2-2. The modified tank design includes an inner chamber which holds the test fluid and which is at the saturation pressure corresponding to the liquid-vapor interface temperature. The outer chamber formed by the pressure vessel can be evacuated to control the pressure differential across the inner chamber wall to assure that any leakage will be out of, rather than into, the inner system. The inner test chamber is a cavity which was formed in the pressure vessel by pouring polyurethane foam over a hemispherical mold at the top and providing an epoxy floor near the bottom. The upper and lower portions of the stainless steel shim stock on the wall were clad with 0.020 in. copper sheet so that only the wetted surface is resistance heated. The polyurethane foam is protected from the vapor by a 10-mil-thick coating of polyvinylchloride.

The ullage heater consists of a hemispherical frame on which 70 feet of 45-mil nichrome V wire is wound. To reduce radiative heat transfer to a minimum, the hemispherical heater was covered on both sides with a mylar film which was aluminized on the outer surface. A copper-constantan thermocouple was mounted on the ullage heating element to monitor the ullage heater temperature.

2-11
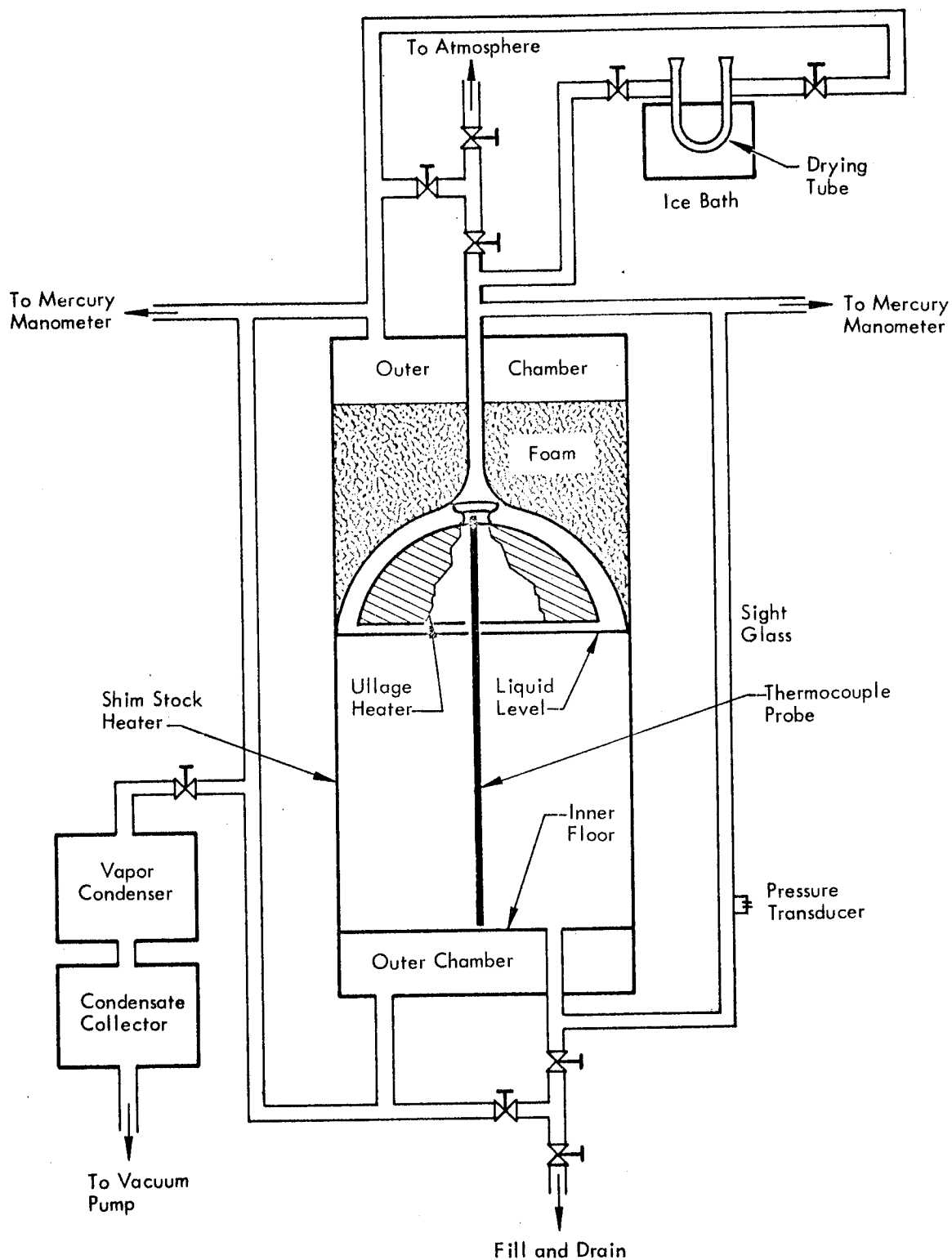
Fig. 2-2 Schematic of Liquid-Ullage Coupling Experimental Apparatus

LOCKHEED MISSILES & SPACE COMPANY

A removable glass drying tube filled with indicating desiccant was placed in the system such that controlled venting could take place through the moisture-absorbing medium. The total amount of vented vapor was determined by accurately weighing the drying tube before and after use.

A thermocouple probe with 18 copper-constantan thermocouples was installed along the centerline of the inner chamber. The probe was constructed from a 5/8-in. o.d. epoxy-glass tube, and the thermocouples were made from 24-gage wire. Also, six thermocouples were mounted on the ullage wall and four were mounted on the shim stock liquid heater. All of the wall thermocouples were made from 36-gage wire. The inner chamber pressure was monitored and recorded using a strain gage pressure transducer mounted below the sight glass.

For each test, the required initial condition was to have the inner tank filled with a saturated liquid in thermal equilibrium with its vapor and the tank. Before testing, all air had to be removed from the system by filling the tank with liquid and boiling it at a low pressure for about 30 minutes. The vacuum pump operated on the ullage during this time and for the 12 hours required to reach thermal equilibrium. When steady state was obtained, the inner chamber was isolated and the test begun.

The liquid and ullage heat rates were the independent boundary conditions for each run. The heat rate to the liquid was obtained as a function of the liquid heater amperage using data from subcooled calibration runs. There were two methods available for the determination of the ullage heat rate. One was to calculate the total energy input by integrating the energy in the liquid and ullage, and then to subtract the calibrated liquid wall heat rate. To facilitate this calculation, as well as to provide values for the heat and mass transfer rates between the liquid and the ullage, an energy balance was written and programmed for computer solution. This program is described in Ref. 5. For most of the test conditions, accurate values for the ullage heat rate could not be obtained using this method because the ullage heat rate was an order of magnitude smaller than the liquid heat rate. However, the alternative method for

2-13

determining the ullage heat rates was quite successful. The conduction losses through the ullage wall were calculated using the measured ullage wall temperature distribution as a boundary condition. These losses and the heat stored in the heating element were subtracted from the total measured power input to the ullage heater to determine the net ullage heat rate.

2.2.2 Experimental Results

The experimental test conditions are summarized in Table 2-1. The average liquid temperature shown is a space-time average and is used to evaluate the modified Grashof and Prandtl numbers for the liquid. The liquid heat rates were obtained from the subcooled calibration runs made with both water and Freon 11. Using the definition of transition from laminar to turbulent boundary-layer flow as given in Ref. 2 ($Ra^*_{TR} = 10^{11}$), the predominant flow regimes in the liquid can be identified. The liquid modified Rayleigh numbers given in Table 2-1 indicate that in all of the water runs, the boundary layer was laminar for more than half the run length. The Freon 11 runs were all predominantly turbulent.

The interfacial heat transfer coefficient on the vapor side is actually a forced convection coefficient, since the flow past the interface was induced by the free convection flow on the walls and ullage heater. For this reason, an average vapor-heater film temperature (defined in Ref. 3) was used to evaluate vapor properties for the calculation of ullage Grashof and Prandtl numbers. Also for this reason, the following forms for ullage Grashof number were selected as the most appropriate for correlation of experimental results:

$$Gr_R = g \beta_v (T_{u\,htr} - T_u) R^3 / \nu_v^2 \qquad (2.27)$$

$$Gr^*_R = g \beta_v q_u R^4 / k_v \nu_v^2 \qquad (2.28)$$

Table 2-1

SUMMARY OF LIQUID-ULLAGE COUPLING TEST CONDITIONS

RUN NO.	RUN TIME (sec)	LIQUID LEVEL (in.)	INITIAL TEMP. (°F)	AVERAGE LIQUID TEMP. (°F)	LIQUID HEAT FLUX (Btu/ft^2-sec)	LIQUID MODIFIED GRASHOF NUMBER Gr_H^*	LIQUID PRANDTL NO, Pr_L	LIQUID MODIFIED RAYLEIGH NUMBER $Ra_L^*=Gr_H^* Pr_L$
					WATER RUNS			
39	1000	11.50	69.9	73.5	116×10^{-3}	0.409×10^{11}	6.4	2.64×10^{11}
40	1000	11.35	70.0	77.0	196	0.82	6.1	5.0
41	1000	11.20	71.3	81.3	274	1.38	5.8	8.01
24	1000	11.25	70.1	70.1	0	0	6.7	0
23	400	11.35	68.9	68.9	0	0	6.9	0
30	400	11.70	72.0	72.1	0	0	6.6	0
52	1000	11.48	68.8	70.3	48.3	0.144	6.7	0.965
57	600	11.32	71.6	72.6	48.3	0.162	6.5	1.05
58	300	11.20	68.5	69.0	48.3	0.134	6.8	0.913
31	1000	11.60	70.8	73.9	116	0.416	6.4	2.66
38	1000	11.60	70.0	73.6	116	0.410	6.4	2.62
37	400	11.97	77.0	78.5	116	0.519	6.0	3.11
42	1000	11.70	70.9	80.4	274	1.34	5.9	7.90
43	1000	11.54	73.0	84.0	274	1.55	5.6	8.70
59	300	11.15	68.3	70.8	274	0.841	6.7	5.64
					FREON 11 RUNS			
66F	1000	11.44	70.3	71.5	14.3	23.0	4.09	94.1
68F	600	11.45	71.3	72.0	14.3	23.2	4.08	94.8
67F	400	11.47	71.0	71.4	14.3	23.0	4.09	94.1
65F	400	11.50	69.7	70.2	14.3	22.9	4.11	94.1
71F	150	11.50	69.4	71.3	200	323	4.09	1320
69F	100	11.47	70.5	71.7	200	324	4.08	1320
70F	290	11.36	63.0	67.0	200	317	4.15	1320
					VENTING RUNS WITH WATER			
62V	1000	11.40	72.7	76.0	116	0.461	6.2	2.86
64V	1000	11.40	74.5	83.0	274	1.49	5.6	8.35

Table 2-1 (Cont.)

RUN NO.	AVERAGE VAPOR FILM TEMP. (°F)	ULLAGE HEAT FLUX[a] (Btu/ft^2 - sec)	ULLAGE VAPOR MODIFIED GRASHOF NO.[b] Gr_R^*	ULLAGE VAPOR GRASHOF NO. Gr_R	ULLAGE VAPOR PRANDTL NO. Pr_v
			WATER RUNS		
39	76.9	-1.35×10^{-3}	0.441×10^5	0	1.08
40	81.1	-2.30	1.34	0	1.08
41	86.6	-3.50	2.02	0	1.08
24	92.3	4.46	0.987	5.72×10^3	1.08
23	91.1	8.88	1.82	5.42	1.08
30	91.8	21.8	6.08	5.97	1.08
52	91.4	5.00	1.20	5.85	1.08
57	94.2	12.2	3.36	6.75	1.08
58	93.9	17.5	3.82	6.50	1.08
31	93.2	4.91	1.48	6.10	1.08
38	86.9	14.5	4.80	3.56	1.08
37	95.2	23.0	9.60	6.83	1.08
42	86.1	6.00	3.67	0.615	1.08
43	99.5	12.6	8.81	9.60	1.08
59	99.7	14.8	4.30	8.86	1.08
			FREON 11 RUNS		
66F	71.8	-2.70	1.02×10^{10}	0	0.72
68F	80.1	2.18	0.803	1.31×10^8	0.72
67F	82.3	4.55	1.62	1.78	0.72
65F	91.2	9.50	2.95	3.03	0.72
71F	71.2	-1.32	0.509	0	0.72
69F	72.7	1.87	0.726	0.110	0.72
70F	83.4	7.60	2.51	2.76	0.72
			VENTING RUNS WITH WATER		
62V	86.6	6.04	2.08×10^5	3.27×10^3	1.08
64V	97.9	5.03	2.89	8.65	1.08

(a) Based on hemispherical ullage wall area
(b) Based on absolute value of ullage heat flux

Table 2-1 (Cont.)

RUN NO.	RUN TIME (sec)	PRESSURE RISE (psi)	ULLAGE MASS CHANGE (lb)	ULLAGE TEMPERATURE RISE (°F)
			WATER RUNS	
39	1000	0.156	6.8×10^{-5}	11.8
40	1000	0.304	13.9	19.3
41	1000	0.485	22.8	29.2
24	1000	0.0238	1.0	5.8
23	400	0.0265	1.2	3.3
30	400	0.0693	2.8	5.2
52	1000	0.0816	3.6	6.7
57	600	0.0909	4.2	6.8
58	300	0.0600	2.9	5.1
31	1000	0.156	6.6	11.1
38	1000	0.189	8.0	13.5
37	400	0.150	5.5	9.2
42	1000	0.511	20.5	27.3
43	1000	0.598	26.0	28.7
59	300	0.211	10.3	15.2
			FREON 11 RUNS	
66F	1000	1.02	343	2.8
68F	600	1.11	328	6.5
67F	400	1.04	289	7.5
65F	400	1.47	313	17.8
71F	150	1.60	525	4.5
69F	100	1.36	455	3.5
70F	290	3.99	1350	14.3
			VENTING RUNS WITH WATER	
62V	1000	0.142	6.4	10.4
64V	1000	0.433	19.2	23.2

The modified Grashof numbers (Eq. 2.28) are based on the calculated net value of the ullage heat flux, thus values are shown in Table 2-1 for the runs where the ullage heater was not used. However, the conventional Grashof numbers (Eq. 2.27) for these runs are shown as zero since the ullage heater temperatures were equal to the vapor temperatures in these cases.

Experimental results were examined to determine the existence and the characteristics of boiling which may have occurred during the high-heat-flux runs. Recorded thermocouple data for Runs 41, 42, and 43 showed that oscillations indicative of boiling occurred at all wall thermocouple locations except the lowest one. These observations imply that boiling started somewhere between 4.25 and 6.5 inches from the tank bottom and persisted along the wall to the liquid surface. Wall superheat for these runs reached a maximum about half way up the wall. Near the liquid surface, the measured superheat was smallest and apparently out of the boiling regime. It is probable that boiling which occurred half way up the wall caused an increase in the boundary-layer velocity and heat transfer coefficient further up the wall, thus reducing the wall temperature. Since boiling may persist at lower values of superheat once it has been established (Ref. 6), the observed superheat is not inconsistent with the presence of boiling near the top of the tank, as implied by the wall temperature oscillations.

Run 59 had the same liquid heat flux as the other boiling water runs, but did not exhibit any boiling characteristics. The wall superheat in this case varied uniformly with vertical distance, as expected for free convection flow with no boiling. Also, there were no wall temperature oscillations during this run. It is concluded that in this case, the increased ullage heat flux and corresponding pressure rise provided sufficient subcooling to prevent boiling.

Three boiling runs (69F, 70F and 71F) were made with Freon 11. The liquid heat rate used for these runs was relatively high and there is no doubt that fully developed nucleate boiling existed in all cases regardless of ullage heat rates.

2.3 COMPARISON OF EXPERIMENTAL RESULTS WITH ANALYSIS

The data from the liquid-ullage coupling experiments with water and Freon 11 have been compared with predictions from the original liquid-ullage coupling model, as modified to consider boiling conditions (Refer to Section 2.1.1). Values of the liquid-vapor interface heat-transfer coefficients and the liquid energy integral used in the model were varied to determine those values which resulted in the most consistent agreement with the data.

The effect of the energy integral on the pressure rise prediction is shown in Fig. 2-3 for Freon 11 and water. The discontinuity in the prediction curves for Run 52 occurs when the stratified layer reaches the tank bottom. This happened at a relatively early time in all of the water runs and in the high-heat-flux Freon 11 runs. The stratified layer reached the tank bottom in about 700 seconds for the low-heat-flux Freon 11 runs (Runs 65F−68F). The value of the energy integral affects the slope of the pressure rise prediction only for times before the stratified layer reaches the tank bottom. Therefore, the energy integral was used to match the slope of the data for the low-heat-flux Freon 11 runs, whereas such a variation had little effect on the slope of predictions for any of the other runs. For the low-heat-flux Freon 11 runs, both the energy integral and h_L were obtained by matching the pressure rise data. However, for these runs, the ullage temperature rise did not provide a solid basis for the selection of h_V. Only the prediction of the mass transfer was used to determine the best value for h_V. The reason for this approach is illustrated in Fig. 2-4. All of the predictions shown are of a reasonable order of magnitude but none has a slope which agrees with the data.

For the water runs, a value of the energy integral was arbitrarily chosen and the corresponding value for h_L determined by matching the pressure rise data (the pressure rise prediction has a negligible dependence on h_V). The value of h_V was then varied until both the mass transfer and the gas temperature rise data were closely approximated by the predictions. Where this could not be done, the value for the energy integral was changed and the process repeated.

2-19

Although the slope of the pressure rise data could be matched in the low-heat-flux Freon 11 runs by selecting an appropriate value of I, the magnitude of the data could not always be matched with the same value of I. This problem is illustrated in Fig. 2-5, where the curves for an I of 0.3 have the correct slope after steady-state stratification is established. For small values of h_L, the prediction is furthest away from the data (curve 1) and the "transient time" is quite large (curve 1 has not yet reached its steady-state slope, which is the same as that for curve 2). As h_L is increased with the same value of I, the prediction agrees more closely with the data. However, curve 2 represents the limiting prediction for an infinite liquid heat transfer coefficient. The interface temperature is very close to the "surface" temperature established by the stratification model. In other words, liquid stratification appears to control the pressure rise under these circumstances. The only way to obtain closer agreement with the data is to change the value of I, thus producing curves 3 and 4. To obtain a prediction which matches the data well and has a slope nearest that of the data, the curve corresponding to an essentially infinite value of h_L was used.

The relative effects of the interfacial heat transfer coefficients on the mass transfer and ullage gas temperature rise are shown for Run 52 in Figs. 2-6 and 2-7. As with the pressure prediction, the slopes of the predictions agree well with those of the data at later times. Figure 2-6 shows that the predicted mass transfer is more sensitive to changes in h_L than h_v. This figure also shows that mass transfer increases with increasing h_v whereas it decreases with increasing h_L. These results are consistent since, in the predictions for Run 52, energy is transferred away from the interface into the liquid and toward the interface from the vapor.

The concave-upward shape of the ullage gas-temperature-rise data for the Freon 11 runs (See Fig. 2-4) may be attributed to the nature of the ullage temperature profiles. The nonuniform ullage temperature profiles shown in Fig. 2-8(a) are characteristic of all the Freon 11 data and do not agree with the uniform profiles assumed in the analytical model. However, the characteristic water data shown in Fig. 2-8(b) do
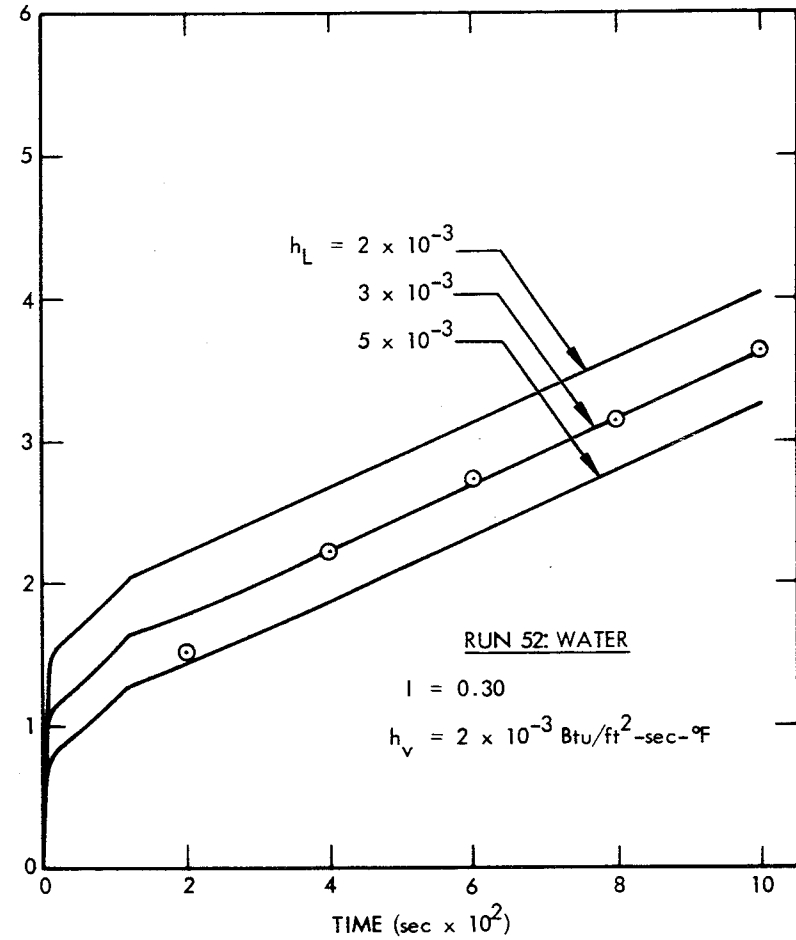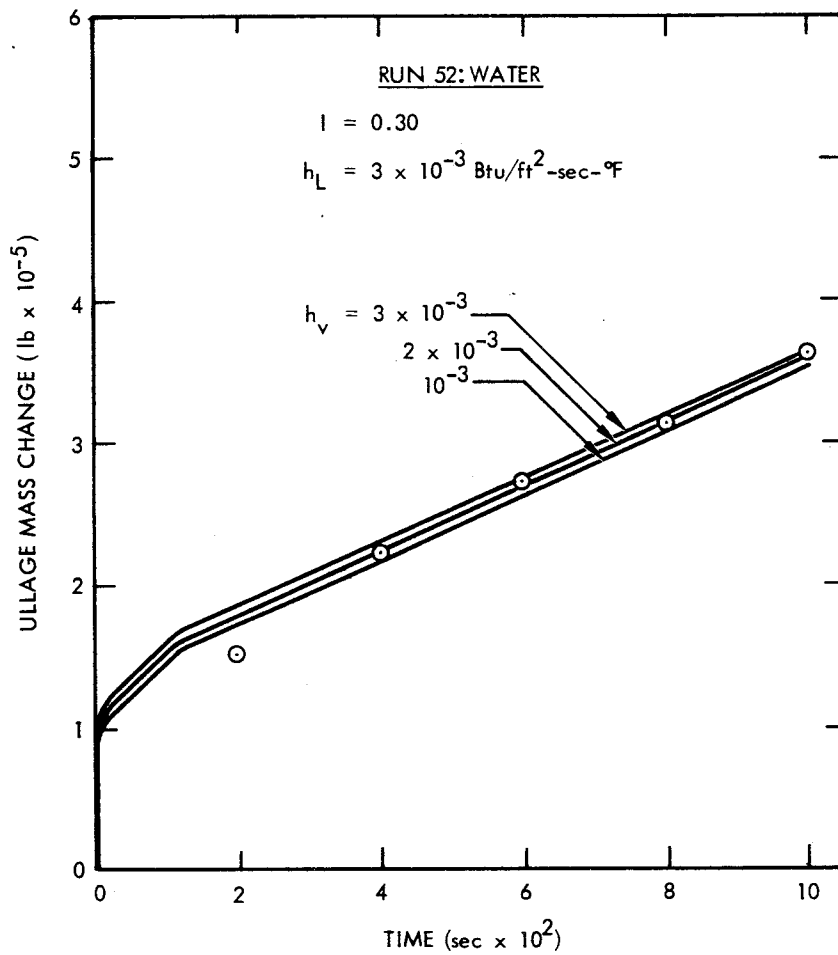
Fig. 2-6 Comparison Between Predicted and Experimental Mass Transfer (Run 52)
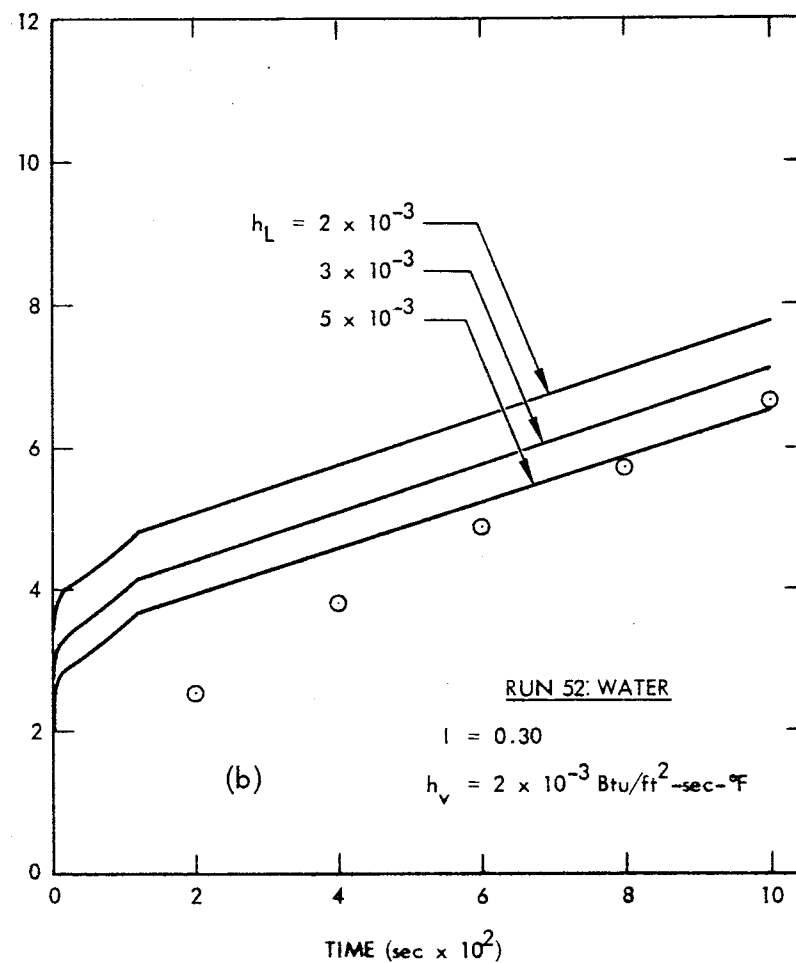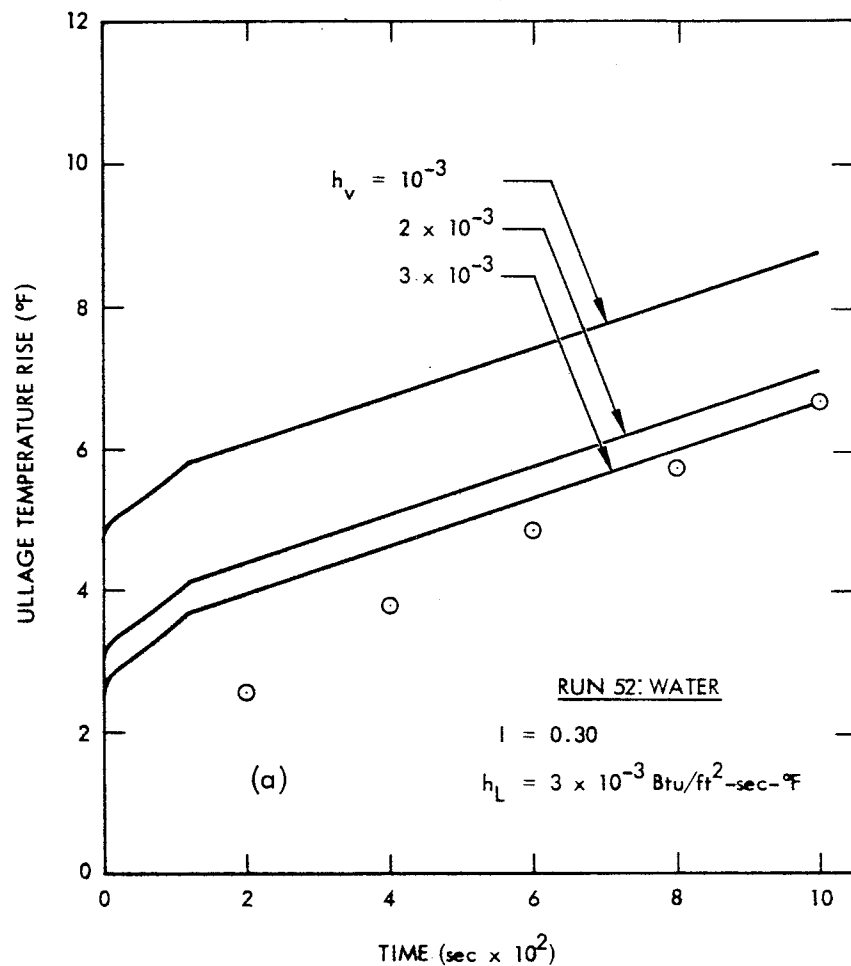
Fig. 2-7 Comparison Between Predicted and Experimental Temperature
Rise (Run 52)

RUN 67F: FREON 11

q_u = 0.00455 Btu/ft²-sec

q_L = 0.0143 Btu/ft²-sec

Gr_R^* = 1.62 × 10¹⁰ Pr_v = 0.72

Gr_H^* = 2.30 × 10¹² Pr_L = 4.09

○ 100 sec
□ 200 sec
◇ 300 sec
△ 400 sec

FILLED SYMBOLS DESIGNATE
SATURATION TEMPERATURE
CORRESPONDING TO
MEASURED PRESSURE

(a)

LIQUID LEVEL

DISTANCE FROM TANK FLOOR (inches)

TEMPERATURE RISE (°F)

○ 200 sec
□ 400 sec
◇ 600 sec
△ 800 sec
▽ 1000 sec

RUN 31: WATER

q_u = 0.00491 Btu/ft²-sec

q_L = 0.116 Btu/ft²-sec

Gr_R^* = 1.48 × 10⁵ Pr_v = 1.08

Gr_H^* = 4.16 × 10¹⁰ Pr_L = 6.4

FILLED SYMBOLS DESIGNATE
SATURATION TEMPERATURE
CORRESPONDING TO
MEASURED PRESSURE

(b)

TEMPERATURE RISE (°F)

Fig. 2-8 Experimental Liquid and Ullage Temperature Profiles

exhibit uniform ullage temperature profiles. The ability of the model to predict the ullage vapor temperature rise seems to be related to how well the measured temperature profiles correspond to those assumed for the model.

During the initial phase of Run 67F (Fig. 2-8a), the gas temperature was less than the interface temperature, implying that heat was transferred from the interface to the ullage gas during this time. At later times, the interface profiles were reversed, and heat was apparently transferred to the interface from the ullage gas. The profiles appear as if the interface temperature was increased initially by stratification, with the ullage heating effect subsequently becoming dominant. It is difficult to explain this ullage temperature history if it is assumed that the ullage heat rate was constant (based on the constant heater power). The temperature rose faster at later times when the heat transfer from the ullage to the interface was probably relatively large. A variable value of h_v could give this result, but it does not seem reasonable that h_v would be smallest when the largest temperature differences existed in the ullage gas. Furthermore, the data as shown indicate that net energy was transferred away from the interface early during the run. This would result in condensation during this time whereas the mass transfer data (obtained from a mass balance on the ullage) indicate that net evaporation occurred. One explanation for this anomaly is that the temperature profile near the interface may have varied in the radial direction. Evaporation near the wall could have cooled the liquid as it flowed past the interface toward the c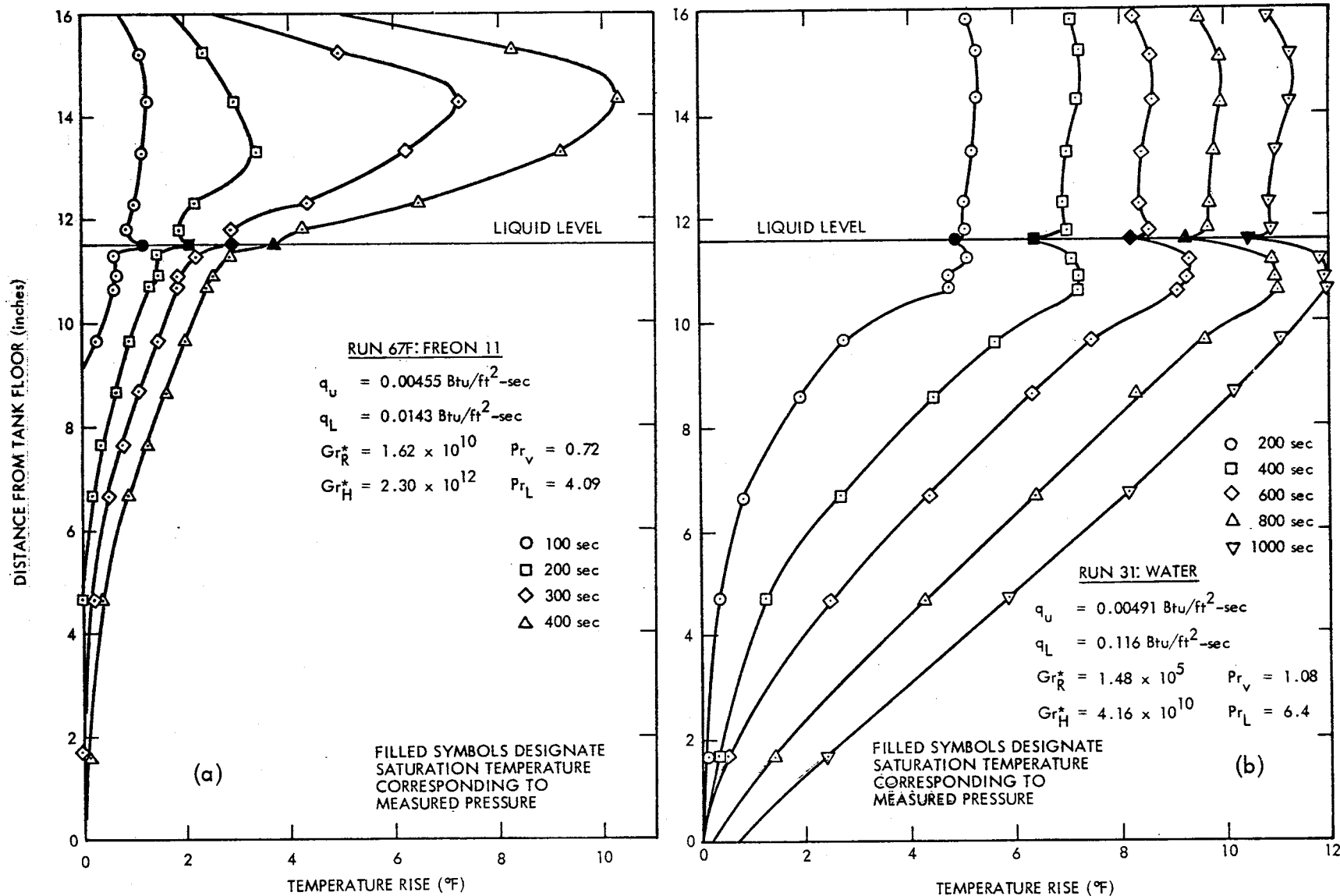enter of the tank. Some vapor could have condensed on the interface near the center, but with the net mass transfer from the liquid to the vapor phase. The liquid-ullage coupling model does not consider a temperature profile variation radially across the interface; however, the net results may still be valid. The correct net mass transfer and pressure rise are obtained using an appropriate average value for the interfacial heat transfer coefficients. However, the ullage gas temperature must be relatively uniform before the model will give a predicted ullage temperature rise which agrees well with data measured on the tank axis.

Figure 2-9 shows the predictions for a venting run which agree quite well with the data. The discontinuity which occurs in the prediction when venting is initiated was

(a)

RUN 62V: WATER

$I = 0.25$

$h_v = 5 \times 10^{-3} \text{ Btu/ft}^2\text{-sec-}°F$

$h_L = 5 \times 10^{-2}$

PRESSURE RISE (psi x 10^{-2})

VENTING STARTED AT 400 sec

$q_u = 0.00604 \text{ Btu/ft}^2\text{-sec}$

$q_L = 0.116 \text{ Btu/ft}^2\text{-sec}$

$Gr_R^* = 2.08 \times 10^5$

$Gr_H^* = 4.61 \times 10^{10}$

$Pr_v = 1.08$

$Pr_L = 6.2$

TIME (sec x 10^2)

(b)

$q_u = 0.00604 \text{ Btu/ft}^2\text{-sec}$

$q_L = 0.116 \text{ Btu/ft}^2\text{-sec}$

$Gr_R^* = 2.08 \times 10^5$

$Gr_H^* = 4.61 \times 10^{10}$

$Pr_v = 1.08$

$Pr_L = 6.2$

RUN 62V: WATER

$I = 0.25$

$h_v = 5 \times 10^{-3} \text{ Btu/ft}^2\text{-sec-}°F$

$h_L = 5 \times 10^{-2}$

ULLAGE MASS CHANGE (lb x 10^{-5})

VENTING STARTED AT 400 sec

TIME (sec x 10^2)

(c)

$q_u = 0.00604 \text{ Btu/ft}^2\text{-sec}$

$q_L = 0.116 \text{ Btu/ft}^2\text{-sec}$

$Gr_R^* = 2.08 \times 10^5$

$Gr_H^* = 4.61 \times 10^{10}$

$Pr_v = 1.08$

$Pr_L = 6.2$

ULLAGE TEMPERATURE RISE (°F)

VENTING STARTED AT 400 sec

RUN 62V: WATER

$I = 0.25$

$h_v = 5 \times 10^{-3} \text{ Btu/ft}^2\text{-sec-}°F$
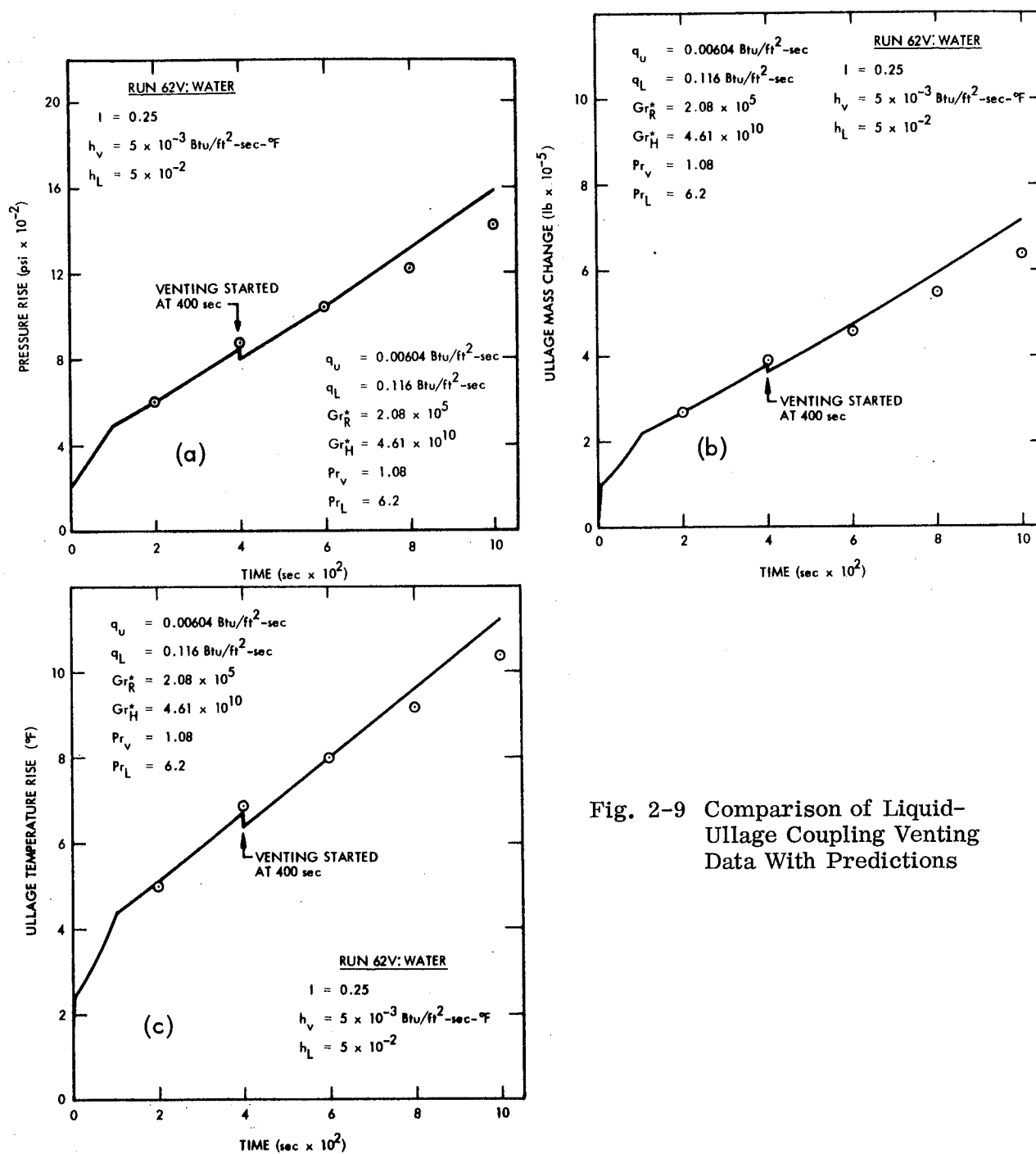
$h_L = 5 \times 10^{-2}$

TIME (sec x 10^2)

Fig. 2-9 Comparison of Liquid-Ullage Coupling Venting Data With Predictions

not observed experimentally and is a function of the value used for h_L. For very large values of h_L, the discontinuity becomes very small, approaching the observed results.

A survey of the available hydrogen liquid-ullage coupling data was made to determine if any of the data were suitable for comparison with the model. To compare the hydrogen data with predictions from the model, data must be available for ullage pressure rise, temperature rise, and interface mass transfer. In addition, all of the boundary conditions must be known. During all of the tests conducted by Lockheed Georgia Co. (Refs. 7 and 8) the fill line was vented to the ullage; thus it is impossible to calculate the interface mass transfer from a mass balance on the ullage. The data obtained by the Martin Co. (Ref. 9) cannot be used because there were no self-pressurized runs during which ullage temperature measurements were made. A reasonable comparison can be made with some of the data obtained from the full-scale S-IV tank tests at MSFC. The data from test 2B satisfy all of the requirements and can be compared with predictions. An approximate value for the ullage heat rate for run 2B was obtained by assuming that the heat rate was proportional to the temperature difference between the liquid or vapor and the outside tank wall. Since the liquid heat rate was obtained independently by an energy balance, the ullage heat rate can be determined. Data for the pressure and ullage temperature were obtained directly, but the interface mass transfer must be calculated from a mass balance on the ullage gas. Since a range of values was measured for both the ullage pressure and temperature, a range of values results for the ullage mass as a function of time. Figure 2-10 compares the data with predictions for various values of h_v and h_L for an energy integral of 0.25. Figure 2-11 shows the effect of a variation in I, holding h_v and h_L constant.

No single combination of parameters will predict pressure, mass transfer, and ullage temperature exactly for this run. In this case, it is necessary to find a compromise which gives the closest approximation of the desired predictions. For example, Fig. 2-10(c) shows that the ullage gas temperature is under-predicted at later times with
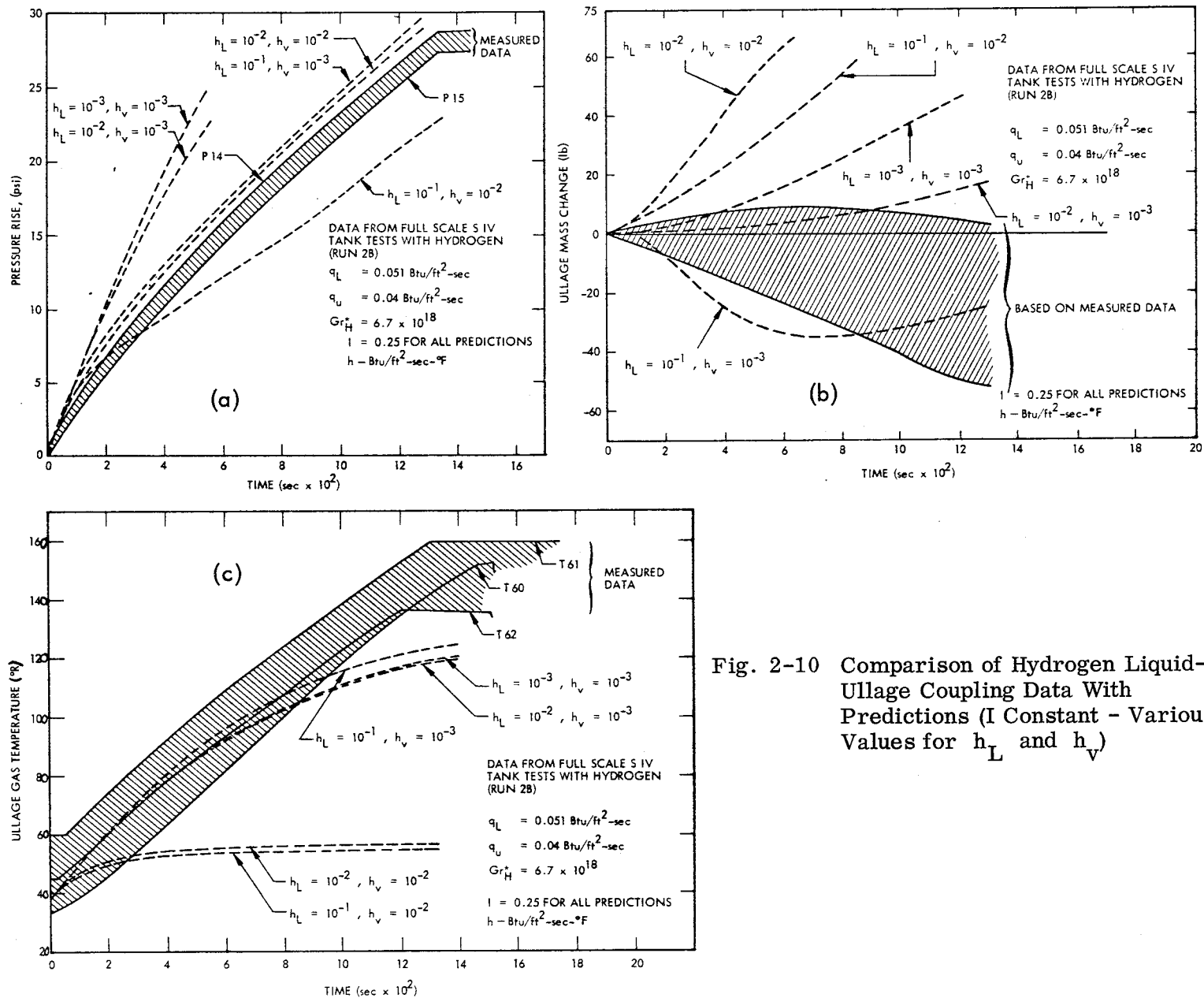
Fig. 2-10 Comparison of Hydrogen Liquid-Ullage Coupling Data With Predictions (I Constant – Various Values for h_L and h_v)
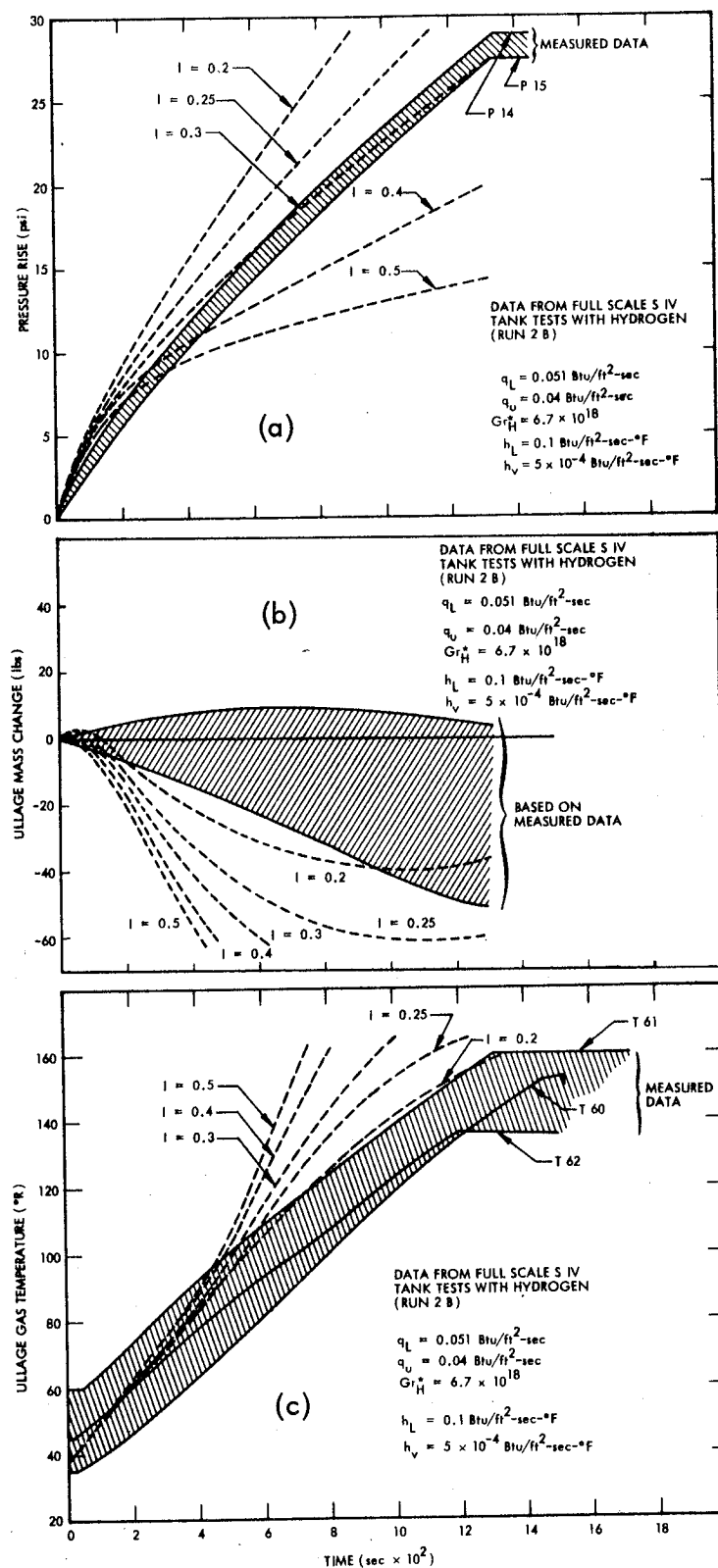
Fig. 2-11 Comparison of Hydrogen Liquid-Ullage Coupling Data
With Predictions (h_L and h_V Constant, Various Values
of I)

2-30

$h_V = 10^{-3}$ and $I = 0.25$. This prediction could be brought closer to the data by increasing I or decreasing h_V as illustrated in Fig. 2-11(c) (h_L has little effect in this case). However, either one of these changes has the effect of moving the mass transfer prediction further away from the data (Figs. 2-10b and 2-11b). A decrease in h_L could be used to counteract the change in the mass transfer prediction, but such a decrease would make it impossible to obtain a reasonable prediction of the pressure rise. (Fig. 2-10a).

2.4 CORRELATION OF RESULTS

Predictions were compared with data from all of the runs, and the values for h_V, h_L and I which produced the best prediction of the data were chosen for each case. These values are given in dimensional and dimensionless forms in Table 2-2. Before correlations could be developed, the significant independent variables were identified and expressed in appropriate dimensionless form. These variables are q_u, q_L, liquid properties, vapor properties, geometry, local acceleration, and the latent heat of vaporization. The geometry was not varied sufficiently in these tests to isolate this effect; therefore geometry parameters such as H/R and L/R cannot be considered for the correlation. This is not believed to be a serious limitation since, for most propellant tanks, any difference in tank geometry probably has a second-order effect on the parameters of interest. This was demonstrated in the case of subcooled stratification when no detectable effect of H/R on the energy integral was found (Ref. 2).

The dimensionless parameters which account for the effects on heat transfer of liquid and vapor properties as well as local acceleration and absolute tank size are the Grashof and Prandtl numbers. Since the vapor Nusselt number did not show any consistent dependence on Gr_R (Ref. 10), the modified vapor Grashof number Gr_R^* was chosen as the appropriate correlating parameter for Nu_V.

Figure 2-12 is a plot of the liquid Nusselt number as a function of liquid modified Grashof number. Although there is considerable data scatter, the inclusion of the

Table 2-2

LIQUID-ULLAGE COUPLING DATA CORRELATION RESULTS

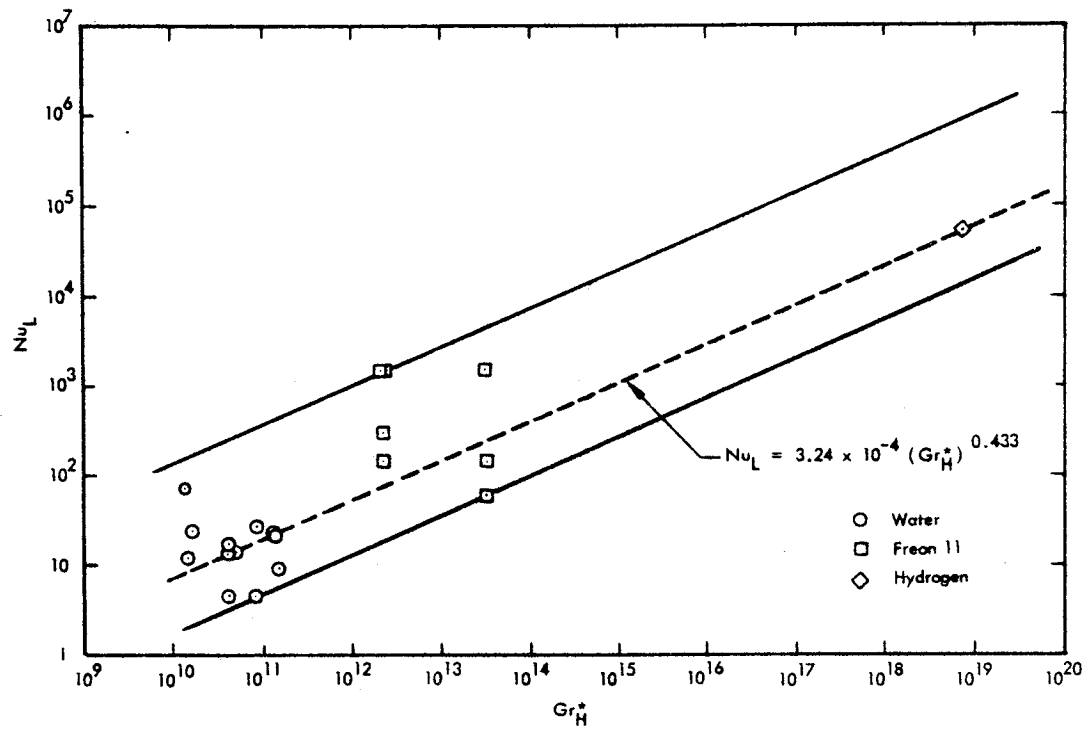| RUN NO.	ENERGY INTEGRAL I	LIQUID SIDE HEAT TRANSFER COEFF., h_L (Btu/ft^2-sec°F)	LIQUID SIDE NUSSELT NO. $Nu_L = h_L R/k_L$	VAPOR SIDE HEAT TRANSFER COEFF., h_v (Btu/ft^2-sec°F)	VAPOR SIDE NUSSELT NO. $Nu_v = h_v R/k_v$
		WATER RUNS			
39	0.2	1×10^{-3}	4.66	1×10^{-3}	158
40	0.2	1	4.66	5	755
41	0.25	5	23.3	0.5	76
52	0.3	2.7	12.7	4	613
57	0.3	5	23.4	10	1520
58	0.3	15	70.3	10	1520
31	0.25	3	14.0	5	760
38	0.3	3.5	16.4	6	926
37	0.2	3	13.9	5	752
42	0.2	5	23.1	5	771
43	0.3	2	9.2	5	750
59	0.3	6	28.1	8	1200
		FREON 11 RUNS			
66F	0.75	10	294	2	643
68F	0.6	5	148	1	324
67F	0.45	50	1470	1	322
65F	0.35	50	1470	0.5	158
71F	0.75	2	59	5	1660
69F	0.75	5	148	10	3290
70F	0.75	50	1480	10	3210
		VENTING RUNS WITH WATER			
62V	0.25	50	233	5	755
64V	0.3	100	466	5	755
		HYDROGEN RUN IN S-IV TANK AT MSFC			
2B	0.25	100	49000	1	4000

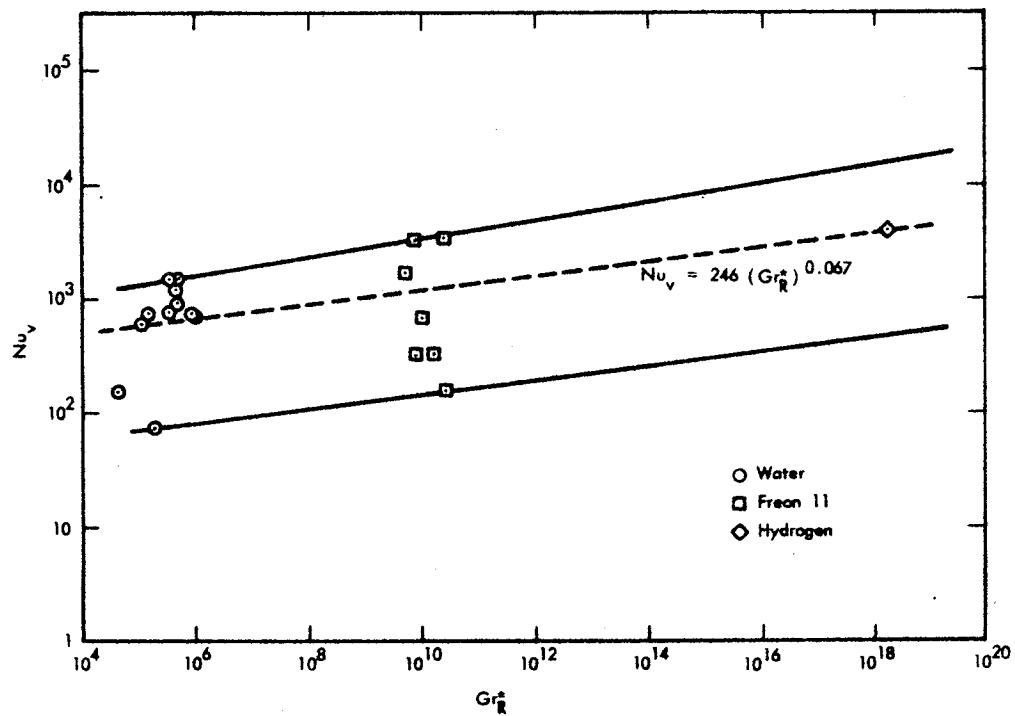Fig. 2-12 Correlation of Liquid-Ullage Coupling Data — Liquid Nusselt Number

Fig. 2-13 Correlation of Liquid-Ullage Coupling Data — Vapor Nusselt Number

Prandtl number as a correlating parameter provides no improvement. This is also true in the case of the vapor Nusselt number correlation (Fig. 2-13). Many attempts were made to reduce the data scatter shown in Figs. 2-12 and 2-13 by the inclusion of other parameter groups, both dimensional and dimensionless, as independent variables. None of these attempts succeeded in reducing the scatter a significant amount, so the simple dependence on only Grashof number has been retained. It is encouraging to note that both the liquid and vapor Nusselt number values obtained from the hydrogen data appear to be consistent with the Freon 11 and water data. The final correlations obtained can be expressed as:

$$Nu_L = 3.24 \times 10^{-4} (Gr_H^*)^{0.433} \qquad (2.29)$$

$$Nu_V = 246 (Gr_R^*)^{0.067} \qquad (2.30)$$

The values of I which were required to match the ullage data with the liquid-ullage coupling model predictions are compared in Fig. 2-14 with the experimental correlation obtained with subcooled-fluid stratification data. The ullage data for water and Freon 11 do not agree particularly well with the subcooled data but seem to follow a similar trend. The one value used to obtain a correlation for the hydrogen run is smaller than the value found to correlate the liquid temperature profiles with bottom heating. If there is a mass transfer effect on the energy integral, it should correlate with some dimensionless form of λ. Several dimensionless "λ groups" which appear in the differential equations describing the liquid-ullage coupling model were considered. These groups contain only fluid properties which are insensitive to temperature variations; thus, for any fluid, there is one value for each λ group. The use of these groups can only shift the set of data for one fluid relative to another fluid. They cannot be used to bring the data points of a particular fluid closer together. The best correlation obtained is shown in Fig. 2-15. The resulting relationship is given by
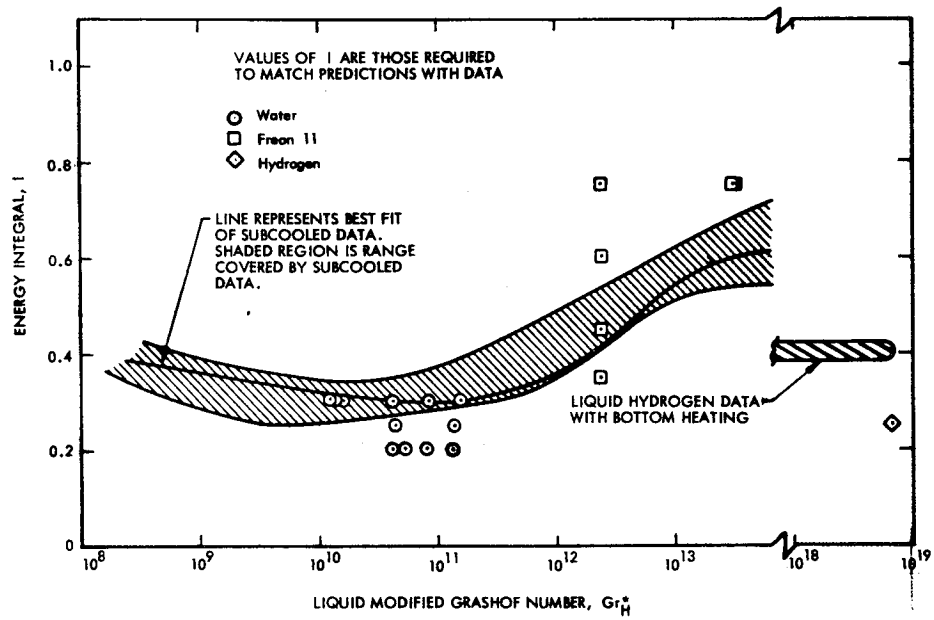
Fig. 2-14 Correlation of Liquid-Ullage Coupling Data-Energy Integral
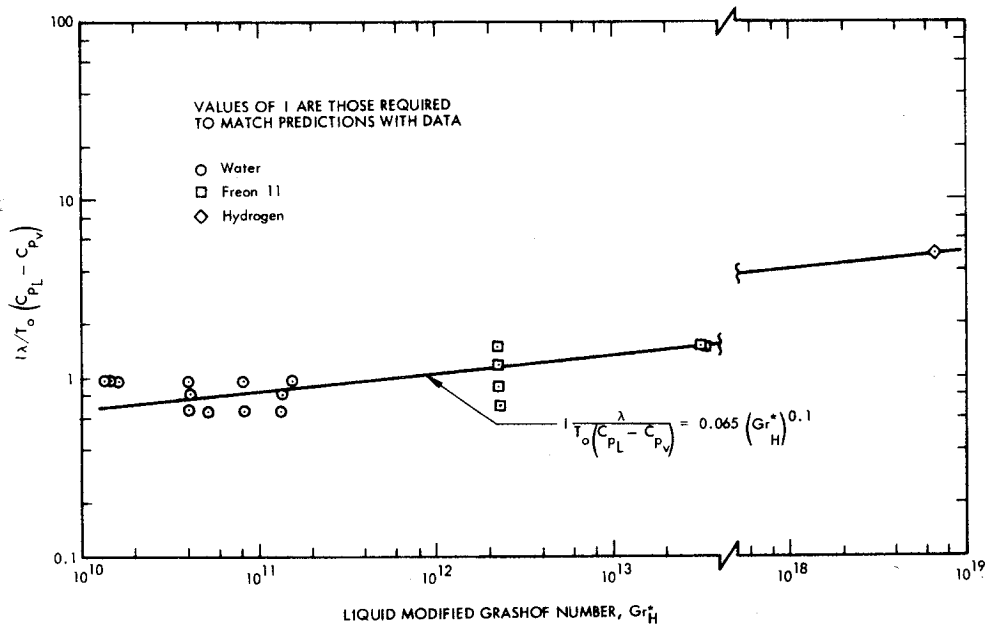
Fig. 2-15 Correlation of Liquid-Ullage Coupling Data

2-35

LOCKHEED MISSILES & SPACE COMPANY

$$I \frac{\lambda}{T_o \left(c_{p_L} - c_{p_v} \right)} = 0.065 \left(Gr_H^* \right)^{0.1}$$ (2.31)

The nature of the data scatter for each fluid and the existence of only one point at a very high value of Gr_H^*, makes it necessary to qualify this correlation. It is recommended that Eq. (2.31) be treated as a preliminary result which requires further confirmation as more data become available, preferably from fluids which cover a wide range of properties.

2-36

Section 3
LOW-GRAVITY INTERFACE STABILITY

An important objective of Phase III of this study was to perform drop-tower experiments to confirm the criteria derived to define the boundary-layer breakthrough problem. The general approach has been to examine analytically the criteria for interface stability and for simulating the boundary layer flow in a large cryogenic tank, and then to design and conduct calibration and drop-tower tests to cover the range of appropriate conditions. A review of the analysis methods and a complete description of the experimental program are presented in this section.

3.1 ANALYSIS

An accurate analytical description of the breakthrough problem is very complex. In principle, the velocity distribution actually existing in the free surface should come from a simultaneous solution of the time-dependent continuity, energy, and momentum equations subject to zero-velocity boundary conditions at solid walls, a zero-shear condition at the free surface, and satisfaction of the contact angle at the wall. At present, however, this rigorous approach is difficult without many simplifications and approximations. An analytical method developed in Phase I of this study to predict free surface shape has been extended to determine the maximum surface Weber numbers which will yield a stable interface. A brief description of this modification is included in this section and a complete description of the computer program is presented in the Appendix. The application of the analytical model for obtaining the appropriate drop-tower test conditions is also described.

3.1.1 Analysis for Limiting Weber Number

The differential equation and boundary condition for the free surface of a liquid in a cylindrical container have been presented in Ref. 1. The equation is

LOCKHEED MISSILES & SPACE COMPANY

$$\frac{1}{r}\frac{d}{dr}\left[\frac{rF_r}{\left(1 + F_r^2\right)^{1/2}}\right] - 2\,F_{rr}(0) - BoF - \frac{We}{2}\,U^2 = 0 \qquad (3.1)$$

with boundary conditions

$$F_r(0) = 0 \qquad (3.2)$$

$$F_r(1) = \cot\theta \qquad (3.3)$$

where F and r are the liquid height (above datum at $r = 0$) and the radial distance, respectively, normalized by tank radius; U is the local surface velocity normalized by the velocity used in the Weber number; and θ is the liquid-wall contact angle. Equation (3.1) has been solved by a method of successive approximations involving integral equations and by numerical integration with iteration of initial values of $F_{rr}(0)$. For a given Bond number and velocity distribution, there exists a limiting Weber number above which numerical solutions cannot be obtained within the mathematical model used. The computer program based on the Runge-Kutta method has been modified to include an iteration scheme to calculate the limiting Weber number.

Observation of the numerical values of $F_{rr}(0)$ as the iteration progressed indicated that only a very small change of $F_{rr}(0)$ values was necessary to go from no solution to a solution. Therefore, the following criterion for defining the limiting Weber number was selected. Let

$$\zeta \equiv \left|\frac{F_{rr}(0)_n - F_{rr}(0)_{n+1}}{F_{rr}(0)_{n+1}}\right| \qquad (3.4)$$

where n and $n+1$ are numbers of iterations. If $\zeta > 2 \times 10^{-8}$ (the computer accuracy limit for single-precision calculations), the iteration with respect to $F_{rr}(0)$ continues with the input Weber number.

If $\zeta \leq 2 \times 10^{-8}$, the Weber number input is greater than the limiting value. For the latter case, a new iteration begins using a lower value of We. This process is repeated until either a prescribed lower-bound value of We is reached or a solution is obtained. The limiting We is considered reached when a solution is obtained for a Weber number which is within five percent of an unstable value. Details of the computer program are presented in the Appendix.

A number of computer runs were made to define the limiting Weber number for the "double-sine" velocity distribution suggested in Ref. 1:

$$U = \begin{cases} \sin\dfrac{\pi}{2}\left(\dfrac{r}{r_m}\right) & , \quad r \leq r_m \\[2em] \sin\dfrac{\pi}{2}\left(\dfrac{1-r}{1-r_m}\right) & , \quad r > r_m \end{cases} \tag{3.5}$$

where r_m is the radial location of the characteristic (maximum) surface velocity. The results are presented in Fig. 3-1, in which the effects of varying r_m and θ are shown. Changing the integration step size, Δr, is seen to have only a minor effect on the results. Other surface velocity distributions, obtained experimentally, have also been used to calculate limiting Weber numbers. These results are discussed in Subsection 3.2.3.

For Bond numbers greater than 200, consistent values of the limiting Weber numbers could not be obtained with either single or double precision calculations. For large Bond numbers and finite Weber numbers, however, the surface tension forces become small compared with the gravitational and inertial forces, and the Froude number becomes the controlling parameter. Therefore, this upper bound of applicability of the model is not considered to be a significant limitation.
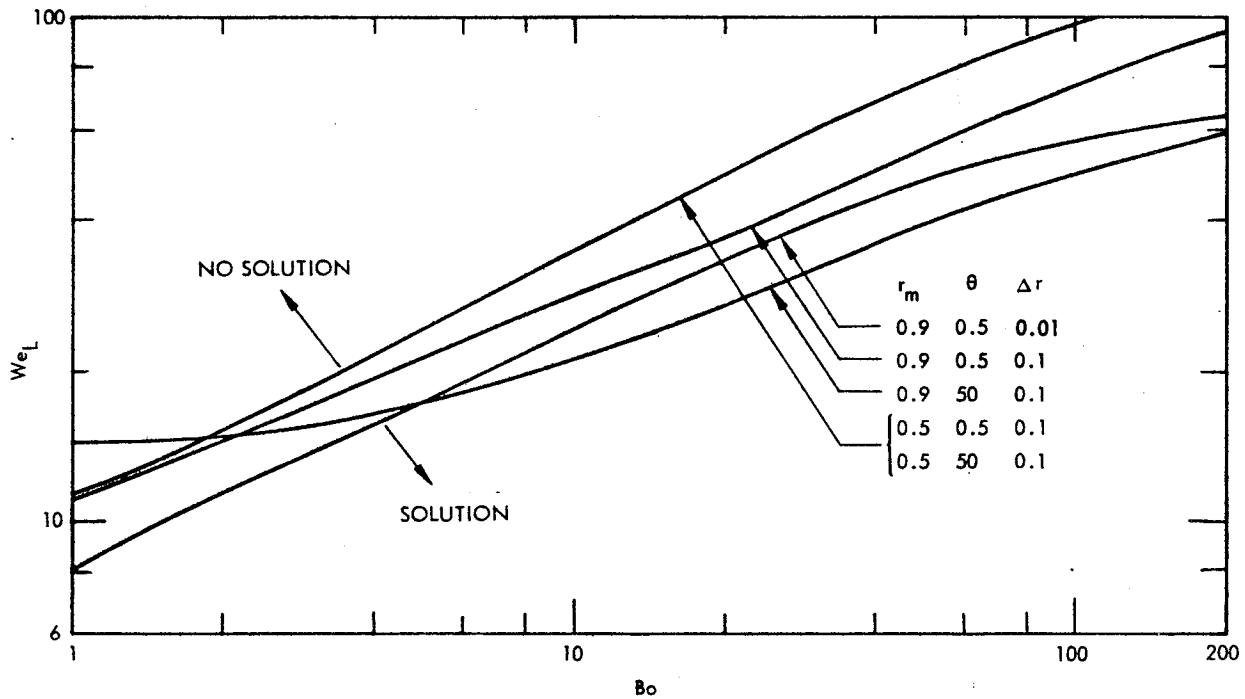
Fig. 3-1 Limiting Weber Number for Double-Sine Velocity Distribution

3.1.2 Analysis of Experimental Velocity Requirements

For small Bond numbers, the integral method of solution of Eq. (3.1) may be used to calculate the limiting Weber number, as described in Ref. 11. A rectangular surface velocity distribution is used to approximate the boundary layer flow:

$$U = \left\{ \begin{array}{ll} 0, & 0 \leq r \leq 1 - \dfrac{\delta_{BL}}{R} \\[3mm] 1, & 1 - \dfrac{\delta_{BL}}{R} \leq r \leq 1 \end{array} \right\} \tag{3.6}$$

For this simple case, a closed-form expression for the limiting Weber number is obtained for $Bo = 0$ and $\delta_{BL} \ll R$:

$$We_{\delta, L} \cong 2(1 + \cos \theta) \qquad (3.7)$$

where $We_{\delta, L}$ is based on the boundary layer thickness, δ_{BL}, and the maximum boundary layer velocity. For fluids with small contact angles, $We_{\delta, L} \cong 4$, where a wall boundary layer is the source of flow. This result was considered to be a general guide to the limiting Weber numbers to be expected.

3.2 EXPERIMENTS

To investigate the validity of the boundary-layer breakthrough criterion obtained from the analysis of Ref. 1, experiments were designed to satisfy the following objectives:

- To obtain experimentally the free-surface radial velocity distribution caused by a convective flow upward along the tank wall
- To investigate the effect on the liquid-gas interface stability in a cylindrical tank of liquid circulation such as that caused by a natural-convection boundary layer
- To determine the Bond number − Weber number combination (i.e., Froude number) to assure an acceptable free-surface rise for the expected full-scale liquid behavior
- To establish the effectiveness of baffles in limiting the boundary-layer "jump" for unstable surface conditions

The experimental program was conducted in two phases. The first consisted of standard gravity tests in which the flow apparatus was calibrated and the liquid surface velocities were measured. The second phase was performed under reduced gravity conditions in the LMSC drop-tower facility at the Santa Cruz Test Base.

3.2.1 Design of Experimental Apparatus

Consider a small-scale experiment of 10 cm radius and 30 cm height to be performed in a drop-tower. If Freon 113 is used as the test fluid (because of its low surface

tension) and a wall temperature difference of 50°F is maintained, a turbulent free-convection boundary layer is obtained whose thickness of 0.5 cm and maximum velocity of 22 cm/sec result in a We_δ value of 18. This condition is sufficient to cause an unstable liquid surface, according to Eq. (3.7). Although the liquid could be heated by using a transparent outer tank filled with warmer liquid, an alternative technique was used which has greater flexibility in that greater Weber numbers could be achieved. This technique was to simulate, insofar as possible, the free-convection boundary-layer velocity and thickness at the free surface with a wall jet whose mass flow could be varied. To size the flow geometry for this experiment, the analysis (Ref. 12) of a plane, semicontained, submerged jet was used. To obtain the desired jet width (0.5 cm) at the surface and for the jet velocity profile to develop into one similar to that of a free-convection boundary layer, the required jet exit was calculated to be 0.2 cm in width, located 2.67 cm beneath the free surface.

The actual dimensions used are shown in Fig. 3-2, which is a schematic of the test tank. Flow from the pump enters the plenum, passes through a filter material to assure flow equalization, and continues into the annular jet fence. Liquid is returned to the pump through a flow-straightener in the tank bottom. A pump capable of a flow rate of 8 gpm was installed and provides We and We_δ values of 2280 and 117, respectively, where We_δ is based on a calculated jet width of 0.54 cm at the liquid surface, and u_m is 1.5 times the average flow velocity at the annular jet exit, based on fully-developed laminar flow. The jet flow rate (velocity) was adjusted by a gate valve in the flow loop. Five flow rates were selected to investigate the limiting value for interface stability as determined from the analysis of Section 3.1.2. The test conditions selected and the corresponding dimensionless parameters are presented in Table 3-1 for the standard gravity calibration runs and the reduced-gravity drop-tower tests. Although water was used as the test fluid in the calibration tests, the Bond and Weber numbers are based on Freon 113 fluid properties in order to be comparable with the flow conditions obtained in the drop-tower tests. The Froude number is the ratio of the Weber to Bond number, and contains no fluid properties.
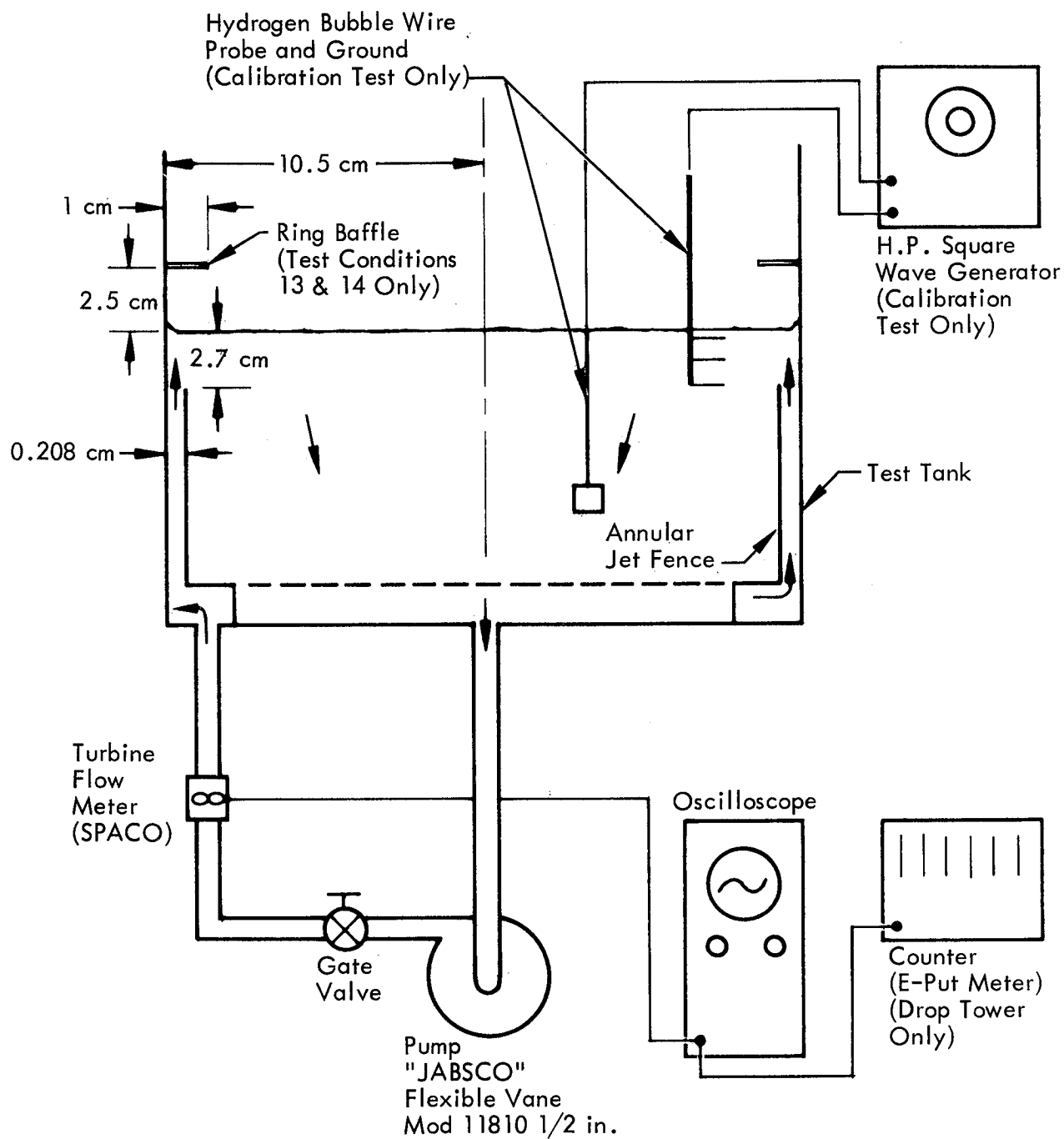
Fig. 3-2 Schematic of Test Tank for Boundary Layer Breakthrough Studies

Table 3-1

SUMMARY OF INTERFACE STABILITY TEST CONDITIONS

Test Condition	Flow Rate gpm	Calculated Jet Velocity (cm/sec)		Acceleration Level	Bond Number	Weber Number			Froude Number
		u_{av}	u_m	g/g_o	Bo	We_m	We_{av}	We_δ	Fr_{av}
1	1.8	8.5	12.7	1	7350	115	51	5.9	0.007
2	2.9	13.6	20.5	1	7350	300	132	15.4	0.018
3	4.9	23.0	34.6	1	7350	855	378	44	0.051
4	6.6	31.0	46.6	1	7350	1550	687	80	0.093
5	8.0	37.6	56.5	1	7350	2280	1000	117	0.132
6	0	0	0	0	0	0	0	0	—
7	1.0	4.7	7.1	0	0	36	15.8	1.8	∞
8	1.8	8.5	12.7	0	0	115	51	5.9	∞
9	2.9	13.6	20.5	0	0	300	132	15.4	∞
10	5.2	24.4	36.7	0	0	962	425	49.5	∞
11	2.9	13.6	20.5	0.1	735	300	132	15.4	0.18
12	2.9	13.6	20.5	0.01	73.5	300	132	15.4	1.80
13	5.3	24.9	37.4	0	0	1000	443	51	∞
14	1.8	8.5	12.7	0	0	115	51	5.9	∞

$$We_{av} = u_{av}^2 R \rho/\sigma \qquad We_\delta = u_m^2 \delta_{BL} \rho/\sigma \qquad We_m = u_m^2 R \rho/\sigma$$

$$R = 10.5 \text{ cm} \qquad \delta = 0.54 \text{ cm} \qquad \sigma/\rho = 14.7 \text{ cm}^3/\text{sec}^2$$

3.2.2 Standard Gravity Flow Calibration Test

As a means for understanding the high-gravity free-surface flow that provides the initial condition for the low-gravity liquid response at engine cut-off, a series of flow calibration tests were performed before conducting the drop-tower tests. This test series had two objectives:

- To examine the overall operational characteristics of the equipment to ensure that the desired performance during the drop tests would be provided. In particular, a correlation of the jet velocity with the gate valve setting and flow meter reading was to be established for later use in the drop-tower tests.
- To examine quantitatively the behavior of the jet flow as it approaches the surface under the high-gravity condition.

The above information was obtained with the aid of a hydrogen bubble flow visualization technique (Ref. 13). The test liquid was distilled water with a small amount of magnesium sulfate added to promote electrolysis and hydrogen gas generation. High-speed motion pictures were taken of the tank under steady-state conditions. The data reduction technique involved tracking selected bubbles, bubble groups, or particles on a frame-to-frame basis using a motion picture film reader.

Figure 3-3 is a diagram of the flow visualization arrangement employed during the flow calibration at standard gravity. The light source was a 35 mm slide projector with a 500 w bulb. Because of the high frame rates and correspondingly short exposure time, more concern was given to light intensity than is usually required with this flow visualization technique. By passing the light beam through two slits, a collimated beam of light, approximately 1 inch high and 1/4 inch thick, was introduced through the tank wall along the diameter. The camera direction of view was normal to the light beam, which is not the optimum angle for viewing sidelighted bubbles. However, this arrangement was necessary in order to limit the flow measurement to the radial direction.
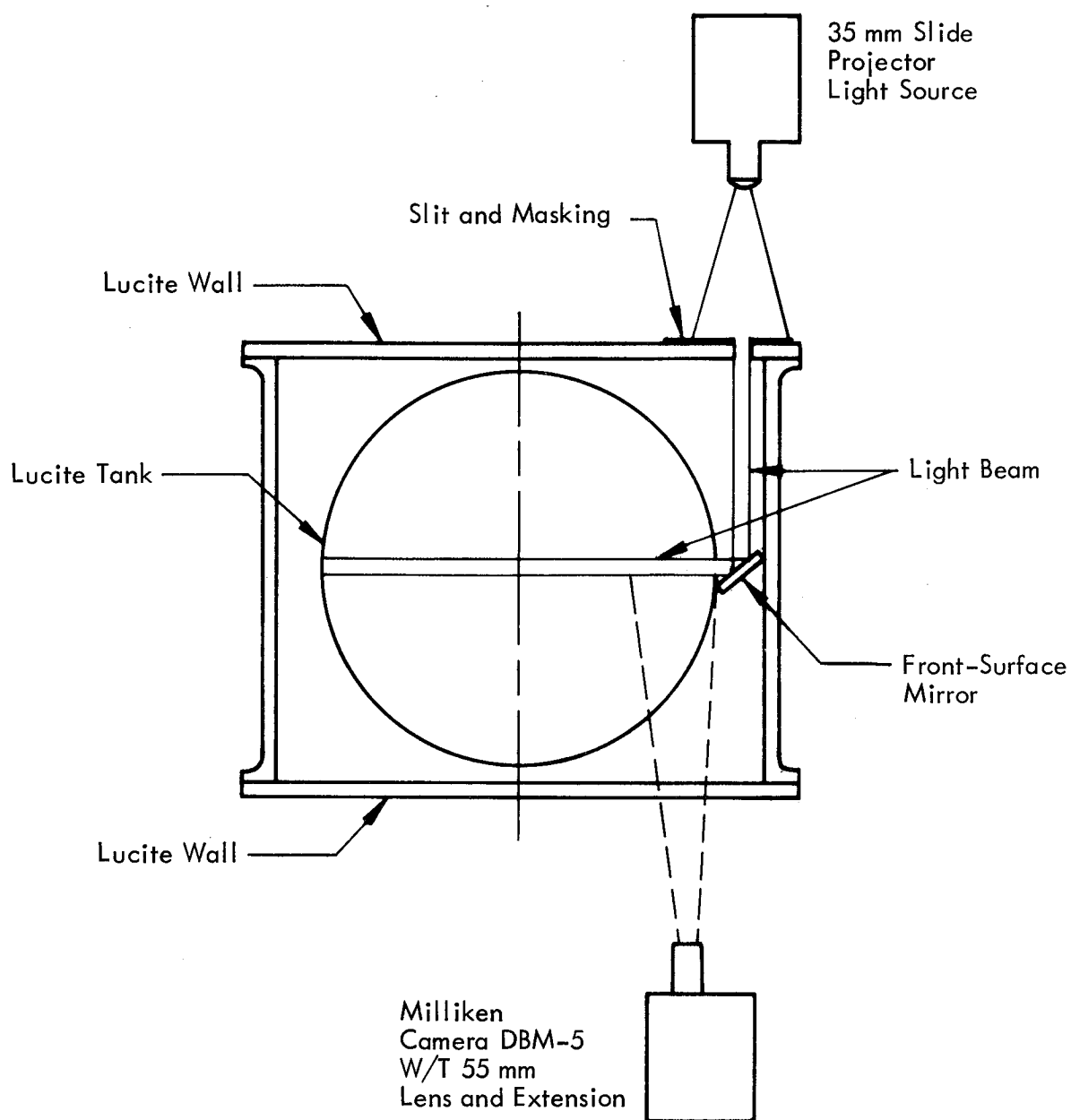
Fig. 3-3 Flow Visualization Apparatus – Top View

Because of the low light level and high frame rates employed, it was necessary to use Tri-X film and overdevelopment to obtain high contrast and a picture from which data could be extracted. Unfortunately, this promoted a grainy structure which reduced the detail that could be seen.

The flow meter output was displayed on an oscilloscope. The scope signal together with the flow meter calibration curve provided the indication of the desired flow rate condition. The pulsed dc voltage to the hydrogen bubble wire was supplied by a Hewlett-Packard square wave generator. This gave excellent on-off characteristics for generating uniform bubble sheets. In all cases except the lowest flow rate runs, the bubble sheets from the probe wires did not retain sufficient integrity to be used as tracking targets. However, the flow was sufficiently populated with small bubbles and particles to allow a flow trajectory to be traced.

A particle displacement from one frame to the next, plus the known framing rate (200 frames per second) yielded local fluid velocities. The displacement values taken were in the radial direction. Care was exercised to select only those particles or bubbles following essentially a radial line. It was intended to obtain velocity information close to the surface; in some instances, however, no particles could be seen in the immediate subsurface region and a particle more deeply submerged was used. No particles more than 0.5 cm below the surface were considered and the great majority were approximately 0.25 cm beneath the surface. A considerable degree of turbulence and vortex activity was present, except during the low flow-rate runs.

The experimental radial velocity distributions are presented in Fig. 3-4. Each data point symbol represents a different tracked particle. It is apparent that considerable scatter in the velocity values is present. Some of this is attributable to the turbulent and nonradial components of the flow. However, much of it is due to the inherent inaccuracy in obtaining the velocity of an object by taking small displacement increments over small time increments. Nevertheless, a trend in the velocity distribution is apparent as indicated by the curve drawn through the data points.
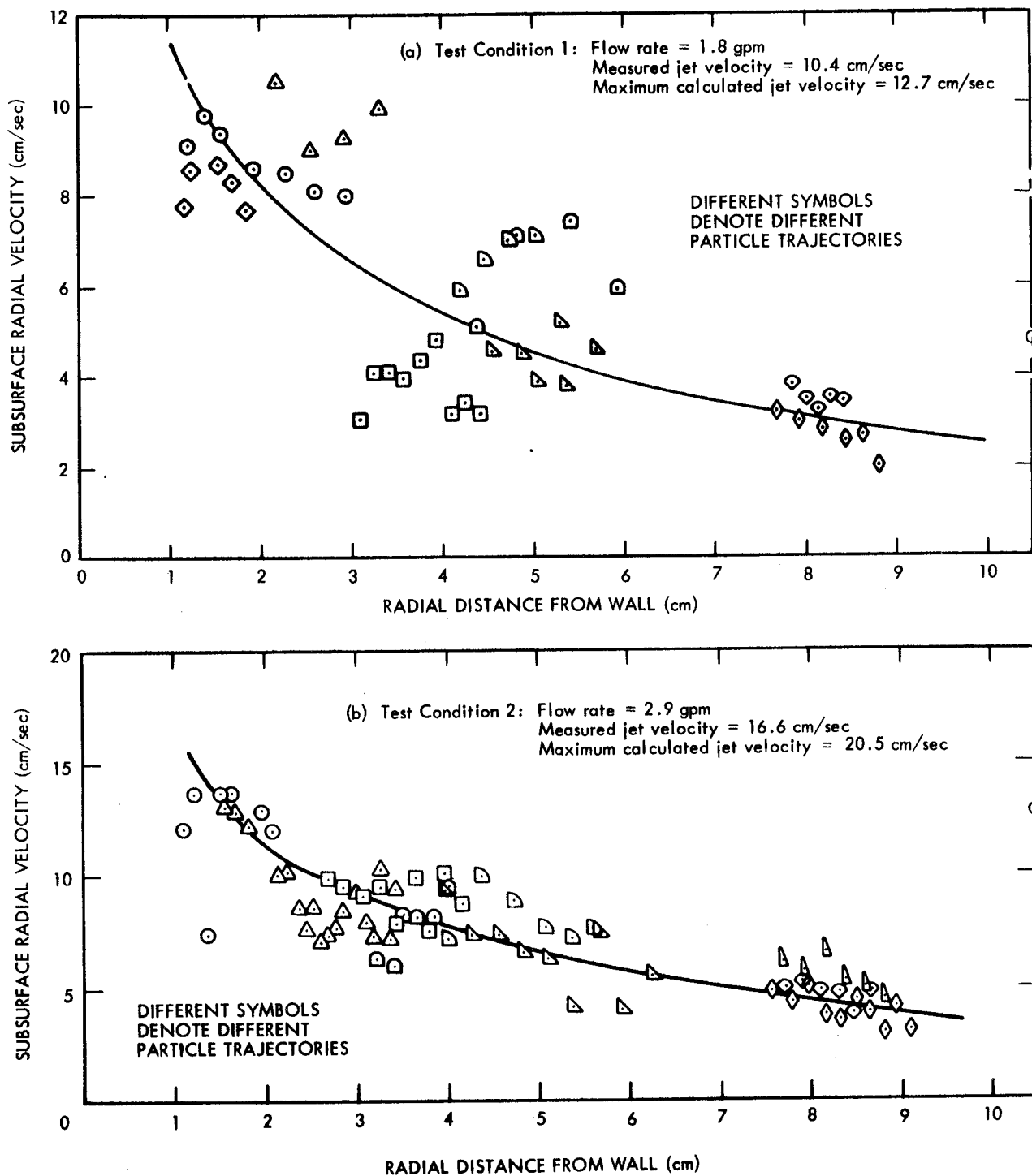
Fig. 3-4 Experimental Subsurface Radial Velocity Distributions

(c) Test Condition 3: Flow rate = 4.9 gpm
Measured jet velocity = 28.4 cm/sec
Maximum calculated jet velocity = 34.6 cm/sec

(d) Test Condition 4: Flow rate = 6.6 gpm
Measured jet velocity = 38.8 cm/sec
Maximum calculated jet velocity = 46.6 cm/sec

(e) Test Condition 5: Flow rate = 8.0 gpm
Measured jet velocity = 46.1 cm/sec
Maximum calculated jet velocity = 56.5 cm/sec

DIFFERENT SYMBOLS DENOTE DIFFERENT PARTICLE TRAJECTORIES
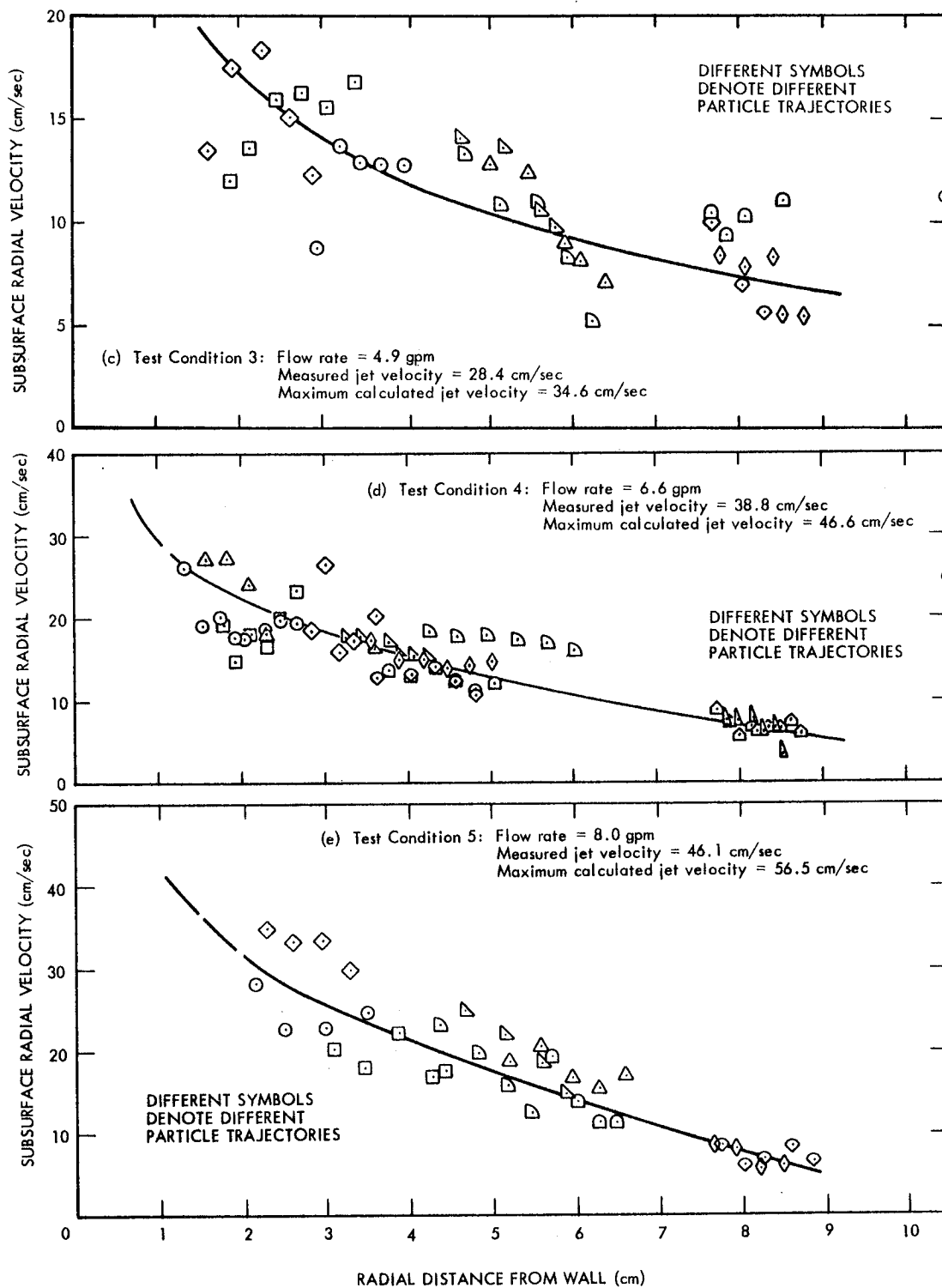
RADIAL DISTANCE FROM WALL (cm)

Fig. 3-4 (Cont)

3-13

As a check on the calculated jet velocity, velocity measurements were taken of the flow issuing from the jet. These data, obtained at the center of the jet, are labeled on the figures as "measured jet velocity." It is noted that these measured values exceed the calculated average velocity in each case, and are less than the calculated maximum values based on a fully developed laminar velocity profile at the jet exit.

Figures 3-5(a) and (b) are sketches of the flow configurations observed during the calibration testing. The low flow condition was less agitated and revealed more details of the flow patterns. Little free surface distortion was present. As the flow approaches the free surface it apparently encounters an adverse pressure gradient associated with the stagnation at the surface and the turning of the flow. In this pressure gradient, a separated region is formed with back flow along the wall and beneath the surface in the form of a stationary vortex.

For the high flow condition, with a Froude number based on average jet velocity of 0.13, the free surface was considerably distorted. A much smaller, almost imperceptible, stagnation region at the junction of the free surface and tank was was observed.

Of the curves in Fig. 3-4, only that for the highest velocity would extrapolate to intersect the tank centerline at zero velocity. It was observed that the flow at the tank center formed a vortex about the tank central axis. Thus the radial flow became a circumferential flow near the center. The radial velocity was assumed to drop to zero over a short distance from the tank centerline.

To demonstrate any similarity among the radial velocity distributions, each of the curves drawn through the data was normalized on the maximum calculated jet velocity and replotted as a function of the normalized radius r. These distributions are shown in Fig. 3-6; a definite degree of similarity is apparent. The choice of the maximum jet velocity as the normalizing parameter is somewhat arbitrary; however, it is the only velocity which is consistently greater than any of the measured subsurface velocities.
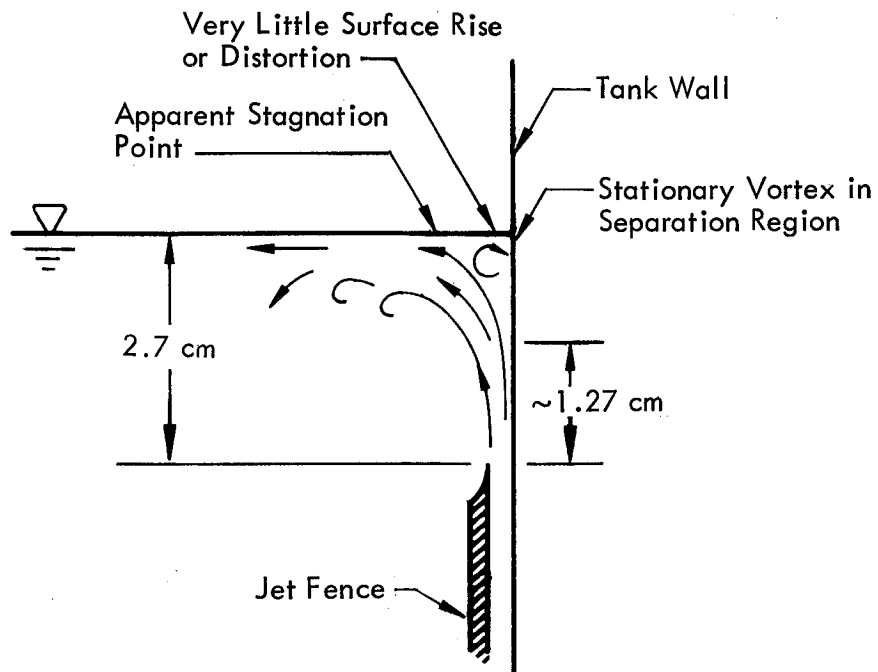
(a) Low Velocity — Condition 1
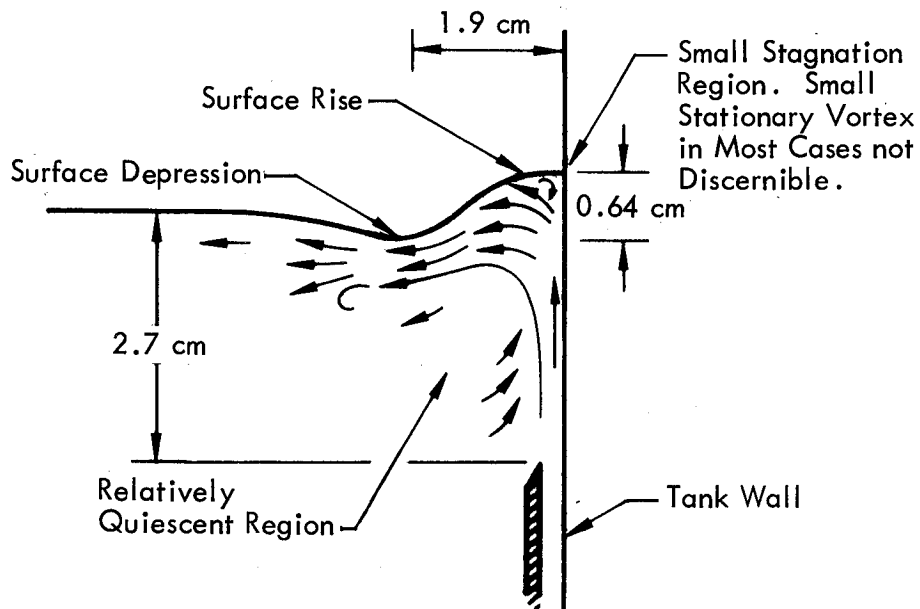
(b) High Velocity — Condition 5

Fig. 3-5 Representative Flow Configurations

3-15

Estimate Based on
Double Maximum
(Vortex at Wall)

Estimate Based on
Single Maximum

$$U = (1 - r^{20})\left[1 - (1 - r)^{10}\right] e^{1.5(r^2 - 1)}$$

Mean of Experimental Data

$u_m = 12.7$

$u_m = 20.5$

$u_m = 34.6$

$u_m = 56.5$

$u_m = 46.6$

NORMALIZED VELOCITY, $U = u/u_m$

NORMALIZED RADIUS, r

Fig. 3-6 Normalized Radial Velocity Distributions

Also shown in Fig. 3-6 are several curves intended to approximate, in various degrees, the experimental data. One of these curves incorporates a stagnation point near the wall, which is intended to approximate the separated region observed in the calibration tests. These various curves are discussed further in Section 3.2.3.

3.2.3 Reduced-Gravity Drop-Tower Tests

Following the flow calibration tests at standard gravity conditions, the test apparatus was installed in the LMSC drop tower for testing under reduced-gravity conditions. Because of its poor wetting characteristics with the Lucite tank w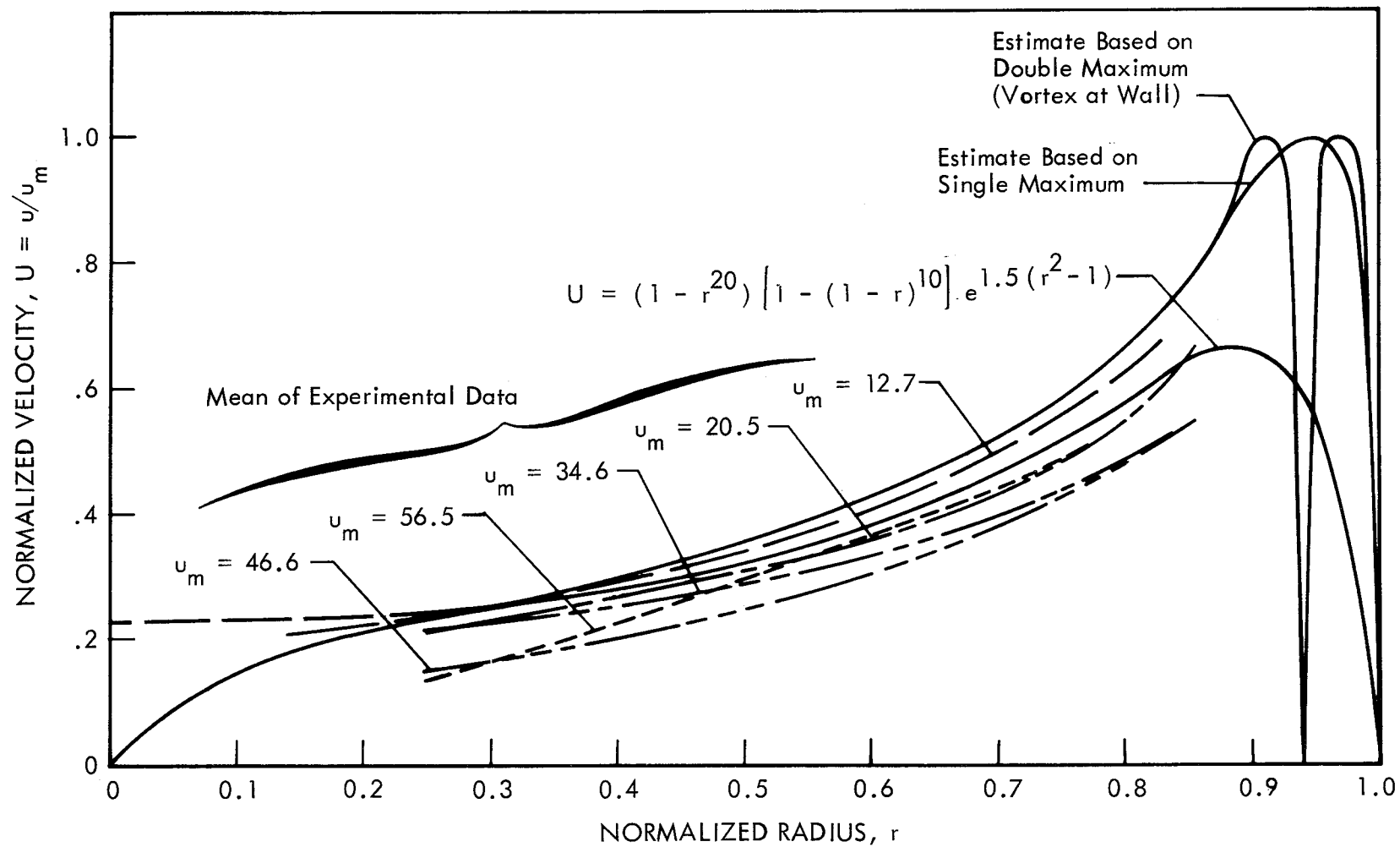all, water was not used for the low gravity drop tests and preference was given to a liquid with wetting characteristics simulating those of a cryogen. Accordingly, Freon 113 (Freon TF) was employed as the test liquid for the drop tests (conditions 6 through 14). Although an alcohol such as isopropyl alcohol would have provided a larger maximum Weber number capability, the Freon was preferred because it is nonflammable. The properties of Freon 113 pertinent to this test are listed below.*

$$\text{Surface tension:} \quad 23.0 \quad \text{dyne/cm (at 25°C)}$$
$$\text{Density:} \quad 1.57 \text{ g/cm}^3 \text{ (at 25°C)}$$

The flow conditions listed in Table 3-1 were established prior to, and maintained throughout, the entire test period of approximately one second. High-speed motion pictures were taken at 200 frames per second. These films constitute the basic set of test data. The low positive accelerations needed for test conditions 11 and 12 were provided by a cold gas thrust system which is integral to the test module of the LMSC drop-tower facility.

The response of the liquid free surface at the tank wall following the reduction in gravity level is indicated in Fig. 3-7 which shows the trajectories of the liquid surface at the tank wall. The run numbers correspond to those on the film records. The displacement is measured from the initial position under standard gravity conditions.
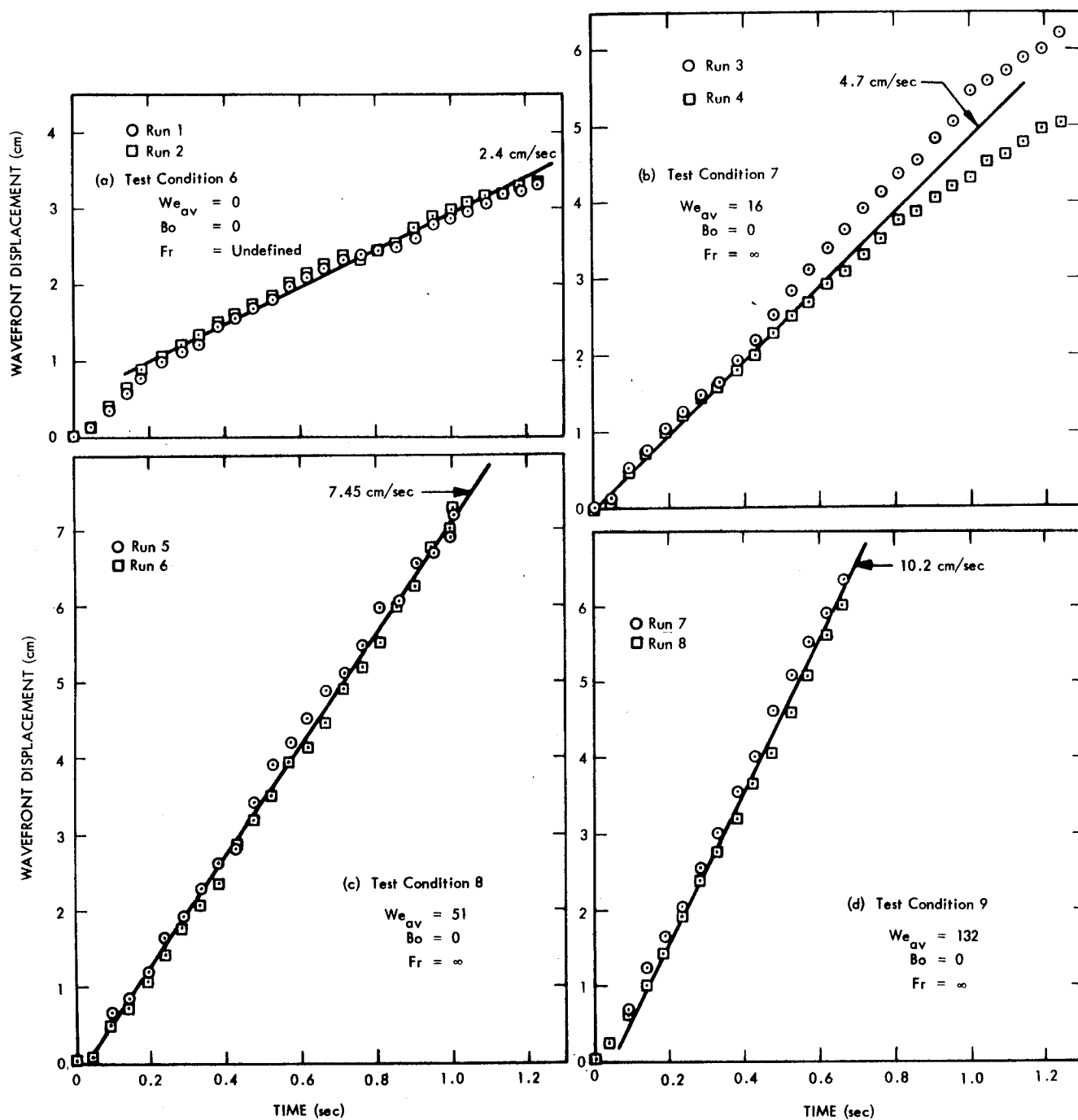
---

*Values taken from DuPont technical bulletins.

Fig. 3-7 Wave Front Trajectories

LOCKHEED MISSILES & SPACE COMPANY
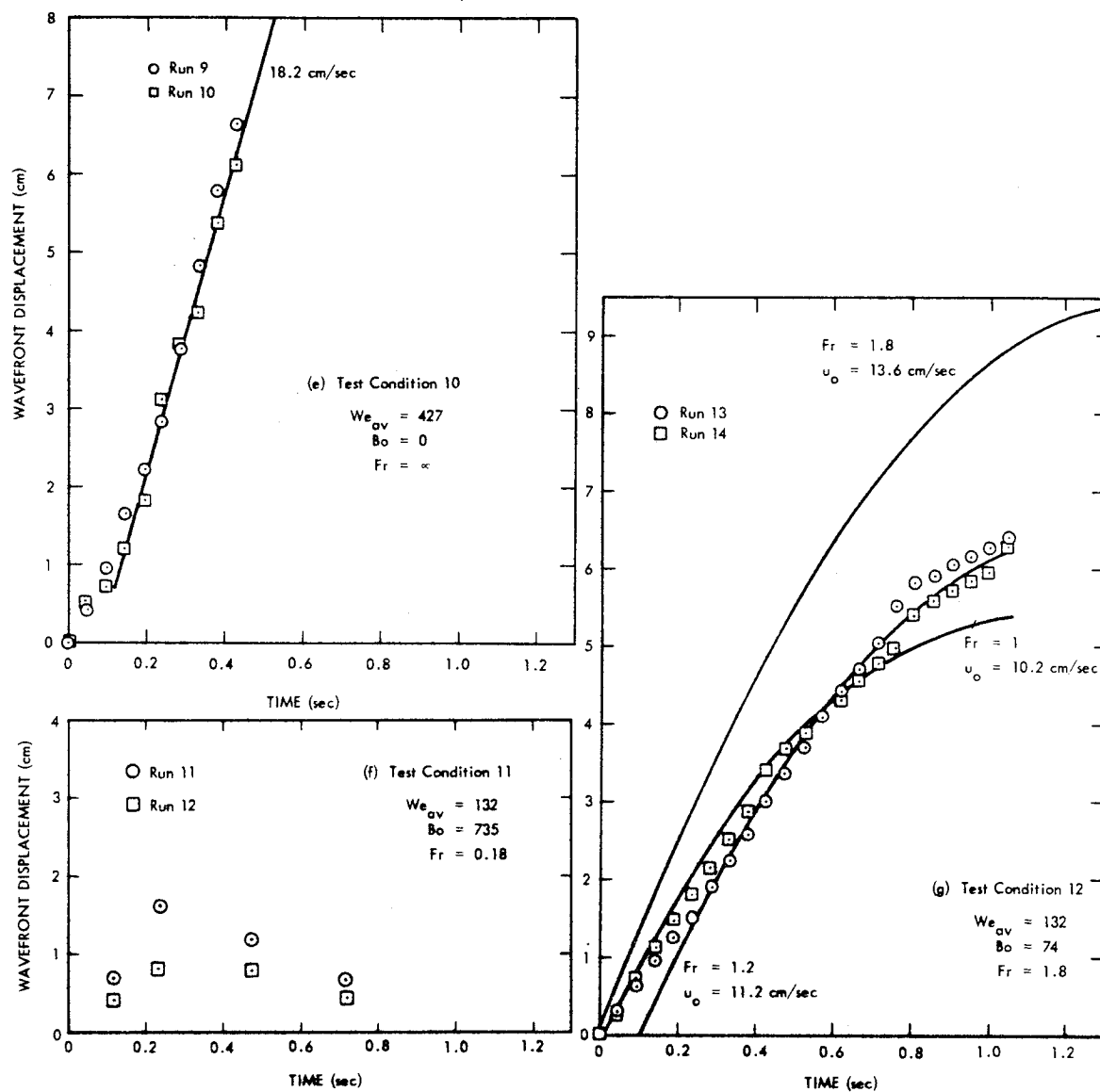
Fig. 3-7 (Cont)

The line through the data points is a "best estimate" of the average velocity of the wave front. In Figs. 3-7(c), (d), and (e), this velocity is less than the predicted value for u_{av} at the jet exit. Figure 3-7(a) shows the wave front trajectory for Bo = 0 and We = 0. For a very low contact angle, such as that for Freon 113 on Lucite, the equilibrium position of the liquid at the wall would be 7 cm above the initial flat interface position. The capillary response time for the liquid to arrive at this elevation can be estimated from the following relation (Ref. 14):

$$\tau = 0.45 \, (\rho \, R^3/\sigma)^{1/2} \tag{3.8}$$

For the tank and liquids used in these tests, this relation yields 4 seconds, so that the observed trajectory in Fig. 3-7(a) is only the initial stage of this liquid orientation. Dividing this response time into the equilibrium distance gives an average reorientation velocity of 1.8 cm/sec. The slope of the line in Fig. 3-7(a) is 2.4 cm/sec which represents the average velocity during the initial liquid rise period.

Figure 3-7(b) represents the lowest Weber number condition examined. Although the transient behavior is not complete in the test time available, an indication of the stabilizing effect of surface tension is evident in the "bending over" of the wall wave trajectory during the last 0.2 seconds of the test.

By comparison, the wave front trajectories for conditions 8, 9, and 10 do not exhibit this tendency toward a stabilized free surface. It is concluded that these high Weber number conditions with zero Bond number (infinite Froude number) produce an unstable condition wherein the free surface was carried away by the momentum of the boundary layer.

The influence of the tank Froude number when a low but nonzero acceleration force is present is shown in Figs. 3-7(f) and (g). In both cases the Weber number was large (the same as that for condition 9), indicating dominance of fluid inertia forces over surface tension forces. However, it is seen that the stabilizing influence of the acceleration level attenuates the wave front velocity.

3-20

The acceleration level for condition 11 was 10 times that for condition 12, and effectively eliminated any appreciable surface rise.

These results indicate that for the flow patterns considered in these tests, the surface tension forces become relatively ineffectual for Weber numbers greater than 16, and that for finite Bond numbers the Froude number is the proper scaling parameter. Under these conditions, the distance through which the liquid interface travels along the wall following a rapid reduction in gravity level is proportional to the dynamic head of the convective boundary layer flow as it approaches the free surface. This may be seen by equating the initial kinetic energy of the flow to the potential energy gained at the maximum height:

$$\frac{u^2}{2\,g_c} = \ell\,\frac{g}{g_c} \qquad\qquad (3.9)$$

or, introducing the Froude number based on tank radius and boundary layer velocity,

$$Fr = \frac{u^2}{gR} = 2\,\ell/R \qquad\qquad (3.10)$$

where ℓ is the maximum liquid travel up the wall. The trajectory of a particle with a known initial velocity can be calculated if the surface tension and viscous forces are small compared with the acceleration force. This has been done for test condition 12 and the resulting curves are shown for several assumed values of initial velocity. The trajectory using an initial velocity corresponding to the calculated average jet velocity (13.6 cm/sec) does not agree as well with the data as one using the average wave front velocity (10.2 cm/sec) measured for test condition 9. The best fit of the data is obtained by using an initial velocity of 11.2 cm/sec, with a lag of 0.1 sec after the change in acceleration. It is possible that some attenuation of the flow velocity and a delay in the free surface response is caused by the vortex observed at the liquid surface wall corner.

Another phenomenon noted in the drop-test films was the appearance of a vertical flow at the tank axis which followed the step change to a low or zero acceleration level. This is a manifestation of a stagnation condition at the tank center due to the radial flow pattern. Although a vortex flow pattern at the tank center was noted in the flow calibration tests during Phase I, it is expected that a certain portion of the boundary layer kinetic energy of the radially directed free surface flow is brought to rest at the tank centerline to produce a region of relatively high pressure and the central flow or "hummock" of liquid noted in the films. The various features of the surface behavior are noted in Fig. 3-8, which is a typical frame taken from one of the drop-tower test films.

For test conditions 13 and 14, a ring baffle was installed in the test tank 2.5 cm above the standard-gravity surface position. The width of the baffle was one-tenth the tank radius, or 1 cm. Two flow conditions at zero Bond number were tested as indicated in Table 3-1. The high Weber number test (condition 13) produced a flow pattern that rose along the wall, encountered the baffle, and was deflected inward toward the tank axis after filling up the region below the baffle. This situation is diagrammed in the following sketch. For this case, the boundary layer flow was not arrested but was deflected into the tank center.
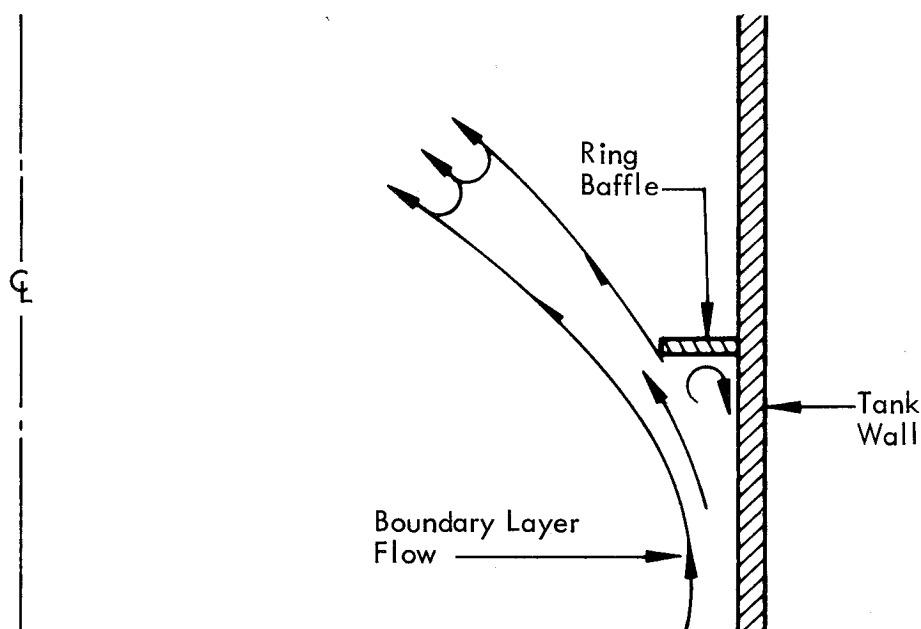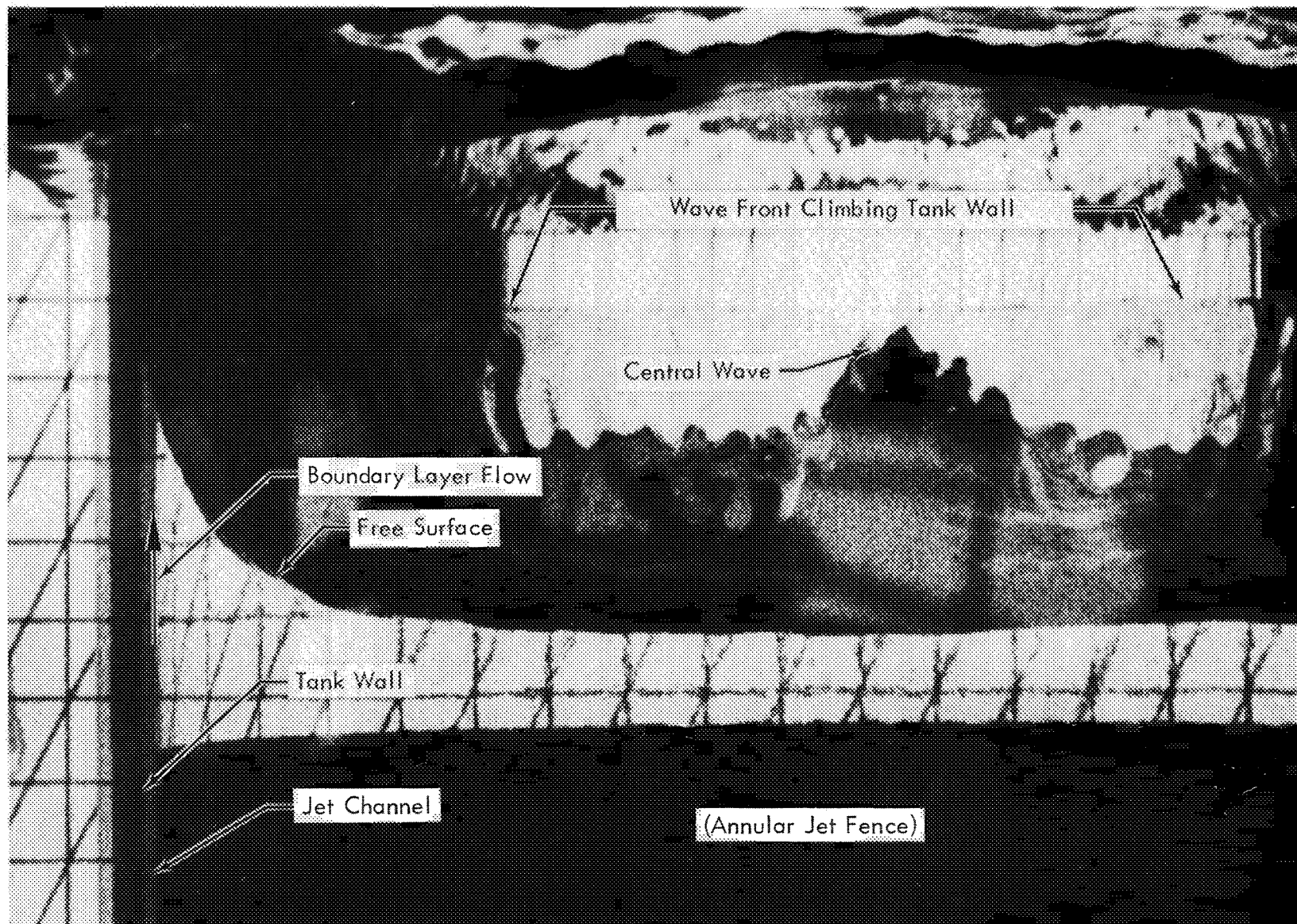
Fig. 3-8 Typical Free-Surface Condition During Drop Test

For the lower Weber number test (condition 14) the ring baffle was more effective in controlling the wall flow. The flow encountered the baffle, filled in the region below the baffle, and apparently stagnated at this point. No indication of flow past the level of the baffle was apparent before the test terminated. A frame from the film of the former test (Fig. 3-9) indicates the "flooded" baffle and the diverted flow directed toward the tank center.

Several approximations of the experimental radial velocity distributions were used in the MENSLM computer program to determine the sensitivity of the predicted limiting Weber number to the normalized velocity distribution used. These results are shown in Fig. 3-10. The limiting Weber numbers obtained from the program are represented by straight lines for $1 \leq Bo \leq 200$ and for the indicated velocity distributions. The lines have the general form $We \propto Bo^{\alpha}$. Also shown are the corresponding limiting Weber numbers for $Bo = 0$. Curve 1 represents the average of the curves shown in Fig. 3-1; curves 2 and 3 are based on velocity distributions shown in Fig. 3-6.

A certain degree of ambiguity is apparent when one attempts to correlate the results of the test program with the analytic predictions. Early in the program, a Weber number stability criterion of 4, based on boundary layer thickness and velocity was determined using a rectangular velocity distribution. The test conditions were chosen based on this criterion. It was subsequently determined that for such cases in which the assumed wall velocity is not zero, much higher limiting Weber numbers are obtained compared with those obtained using the distributions of Fig. 3-6 which have zero velocity at the wall. Thus, the stability criteria shown in Fig. 3-10, based on the approximations to the experimentally determined subsurface radial velocity distributions of Fig. 3-6, are lower than the Weber numbers investigated during drop testing.

The precise relation between jet velocity (average or maximum) and the maximum or characteristic subsurface velocity is not entirely clear, although the similarity between

3-24
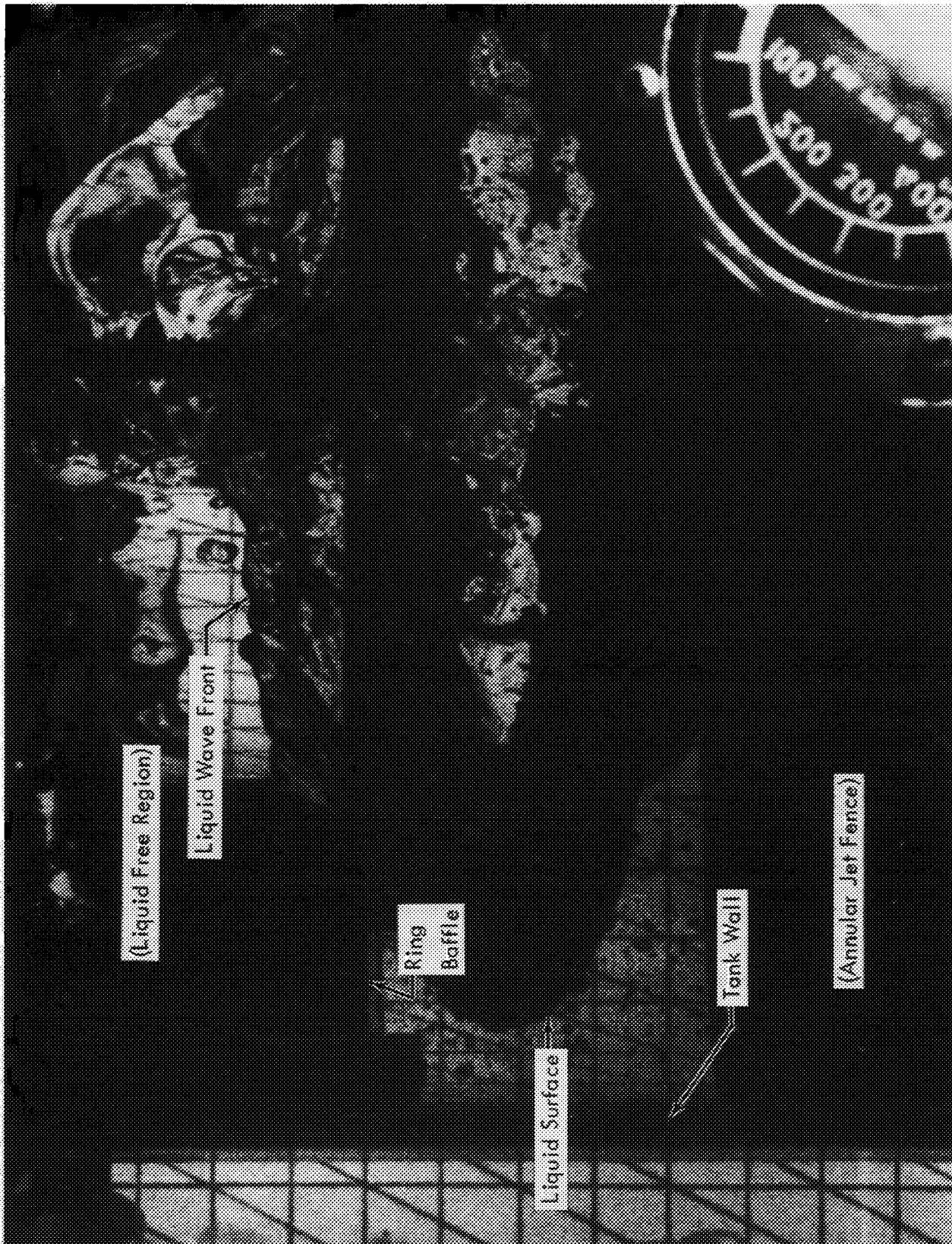
Fig. 3-9 Free Surface Condition During Drop Test With Baffle

LOCKHEED MISSILES & SPACE COMPANY

individual normalized velocity distributions has been demonstrated. Examination of Fig. 3-6 indicates that a reasonable approximation of the maximum radial component of the subsurface velocity is

$$u_s = 0.67 \, u_{jet_m}$$

$$u_s = 0.67 \, u_m$$

Shown in Fig. 3-10 are the two experimental points obtained at reduced gravity levels and the condition at zero gravity and lowest We value (condition 7). These points are shown for three assumed maximum surface velocities: $u_s = u_m$, $u_s = 0.67 \, u_m$ and u_s = measured wavefront velocity during zero-gravity (from Fig. 3-7). Except for the test at $Bo = 740$, the resulting Weber numbers are greater than the limiting values predicted by the program. However, in both these cases a tendency toward free-surface stability was noted. Therefore, the predictions of the MENSLM program are apparently conservative.

Figure 3-10 can be considered a map of the various force-balance regimes considered in this investigation. All points to the left of the $Bo = 1$ line are in a surface-tension dominated regime with respect to gravity forces. In this region, those points below $We_s = 4$ are also surface-tension dominated with regard to fluid inertia forces and the free surface is "stable" in the common sense of the term; that is, a free surface exists. Above this region no free surface exists and one can expect inertia forces to carry away the free surface. To the right of the $Bo = 1$ line is a regime dominated by gravity-induced body forces. The term stability in this regime must be modified to include the effect of gravity. The curve on Fig. 3-10 obtained from the MENSLM program for $1 \leq Bo \leq 200$ would indicate that a combination of surface-tension and gravity forces produce a stability limit. In this region, it is largely the gravity forces that govern the condition of free surface stability. This is probably the reason for the upward trend of the stability limit curve in this region. Points that lie along the line $Fr = 1$, but are above the "stability limit" curves, are stable if liquid-rise heights at the wall that are equal to the tank radius are acceptable. In this case, the free surface is stabilized by the local gravity level.

CURVE 1: AVERAGE OF VALUES FOR DOUBLE-SINE DISTRIBUTION ($U_m = 1$ at $r_m = 0.5$ to 0.9)

2: $u = (1 - r^{20}) [1 - (1 - r)^{10}] e^{1.5(r^2 - 1)}$ ($U_m = 0.66$ at $r_m = 0.89$)

3: BASED ON ESTIMATED, SINGLE-MAXIMUM DISTRIBUTION WITH $U_m = 1$ at $r_m = 0.95$

Fr BASED ON MAXIMUM SURFACE VELOCITY

$We = u_s^2 R \rho / \sigma$

$Fr = 1$

$Fr = 10$

$Fr = 0.1$

$0.01 \, g_o$

$0.1 \, g_o$

$Bo = 0$

EXPERIMENTAL CONDITIONS, ASSUMING
○ $u_s = u_m$
□ $u_s = 0.67 \, u_m$
◇ $u_s =$ MEASURED WAVEFRONT VELOCITY IN ZERO-GRAVITY
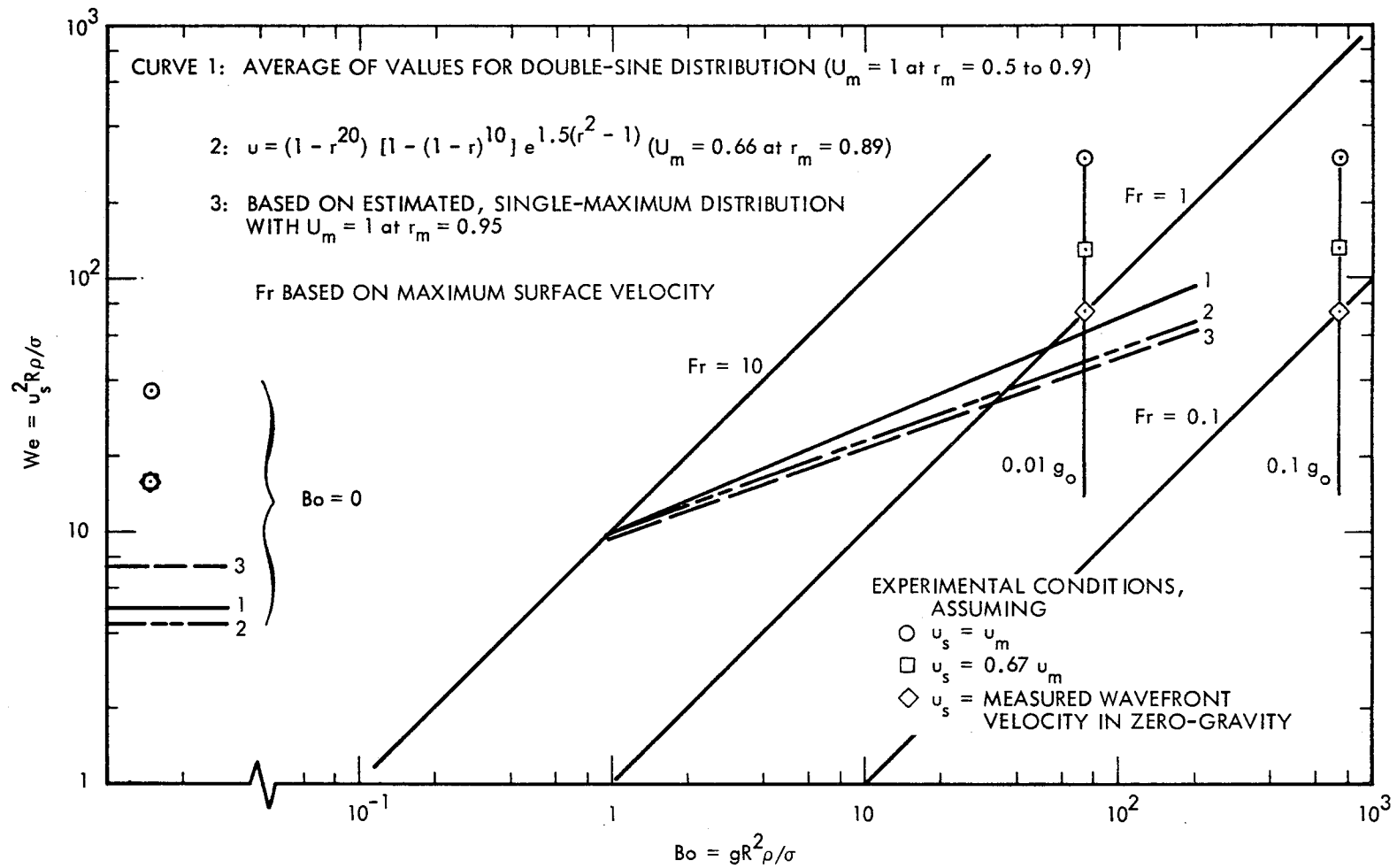
$Bo = gR^2 \rho / \sigma$

Fig. 3-10 Limiting Weber Number Correlations

It should be pointed out that the effect on the subsurface velocity distribution of a change in the surface shape resulting from the reduced gravity level has not been determined. It is reasonable to expect that the change in surface shape will have an effect on the surface velocity distribution, which is not accounted for in the analysis. Also, for a highly wetting liquid where the interface becomes highly distorted at the container wall during low gravity conditions, a small computing mesh size should be used to define adequately the free surface limit. Mesh sizes (integration step size Δr) of 0.01 and 0.1 were used to obtain the results shown in Fig. 3-10.

3.3 APPLICATION OF EXPERIMENTAL RESULTS TO VEHICLE DESIGN

Application of the results of this experiment to vehicle design is relatively straightforward if a characteristic boundary layer velocity can be determined. The velocities characteristic of natural convection boundary layers in large cryogenic stages at standard or larger gravity conditions yield very large tank Weber numbers. This indicates an inertia-dominated regime after the high vehicle acceleration is reduced to zero. Accordingly, surface tension forces will be of little aid in providing the stabilizing force needed by the free surface to contain the boundary layer flow.

For a large cryogenic stage such as the S-IVB, an average velocity on the order of 1 ft/sec in the convective boundary layer in the region of the liquid free surface has been calculated (Ref. 15). The Weber number is 9.3×10^3, based on a tank radius of 130 inches with liquid hydrogen as the propellant. This is much greater than the Weber number of 50 which was seen to result in an unstable condition in the test tank. In the absence of an acceleration-induced body force on the liquid, the boundary layer flow would continue through the free surface into the ullage.

Two means for containing the boundary layer liquid are baffles, to divert the flow and dissipate the associated kinetic energy, and stabilization of the flow with positive vehicle acceleration. If it is desired to keep the wall wave rise below one tank radius, the Froude number relation of Eq. (3.10) yields a required acceleration level of $1.43 \times 10^{-3} \, g_o$ for the S-IVB stage.

Section 4
CONCLUSIONS

An extensive test program was conducted using noncryogenic fluids to study the pheno-
menon of liquid-ullage coupling. Predictions of pressure rise, interface mass trans-
fer and ullage temperature rise obtained from the extended liquid-ullage coupling model
agree well with the data when appropriate values for h_V, h_L, and I are used.

The liquid-ullage coupling model successfully predicted the results of tests conducted
with controlled ullage venting.

The extended liquid-ullage coupling model which accounts for the influence of nucleate
boiling in the liquid free-convection boundary layer yields predictions which agree well
with data obtained from tests with boiling.

Available hydrogen data were surveyed and the results from one of the tests conducted
at MSFC on a full scale S-IV tank were found to be suitable for comparison with pre-
dictions from the liquid-ullage coupling model. Values for h_V, h_L and I were
obtained which yielded predictions agreeing well with the data.

The results of the noncryogenic tests and the usable hydrogen data were used to develop
the following correlations for h_V, h_L and I :

$$Nu_L = 3.24 \times 10^{-4} \left(Gr_H^*\right)^{0.433} \tag{4.1}$$

$$Nu_V = 246 \left(Gr_R^*\right)^{0.067} \tag{4.2}$$

$$I = \frac{0.065\, T_o\, (c_{p_L} - c_{p_V})}{\lambda} \left(Gr_H^*\right)^{0.1} \tag{4.3}$$

4-1

The correlation for I is qualified as preliminary since only one data point could be obtained from the hydrogen tests. As more data become available, further confirmation of this correlation will be possible.

Free surface radial velocity distributions have been determined for a range of simulated convective boundary layer velocities. It has been shown that, when normalized, these distributions have a similar form.

Based on this normalized velocity distribution, a free surface stability criterion for a tank bond number of zero is $We_{av} \leq 4$.

For low but nonzero positive tank acceleration $(0 < Bo < 100)$, the stabilizing effect of the gravity level is added and the limiting stability criterion may be approximated by

$$We_{av} \leq 10 \, (Bo)^{0.35} \quad \text{for} \quad 0.1 \leq Bo \leq 100$$

At tank Bond numbers greater than 100, the effect of surface tension is negligible and a proper scaling parameter is the Froude number. The jump height is

$$\ell = R \, Fr/2 \qquad (4.4)$$

where ℓ is the height along the wall that the convective boundary layer momentum will carry the liquid.

Experimental data indicate that these Weber number stability criteria are conservative and that the Froude number relation is valid in the range of tank Bond numbers investigated.

For large Weber number flows $(We_{av} > 400)$ at zero Bond number, an unsubmerged ring baffle of width $0.1R$ deflected the wall flow but did not arrest it. For $We_{av} = 50$, some effectiveness in stopping the wall flow was observed. These results apply to tanks with a boundary layer thickness at the free surface of the order of five percent of the tank radius.

Section 5
REFERENCES

1. Lockheed Missiles & Space Co., Analytical and Experimental Study of Liquid Orientation and Stratification in Standard and Reduced Gravity Fields, 2-05-64-1, Contract NAS 8-11525, Sunnyvale, Calif., Jul 1964

2. -----, Analytical and Experimental Study of Stratification and Liquid-Ullage Coupling, 2-05-65-1, Contract NAS 8-11525, Sunnyvale, Calif., Aug 1965

3. -----, Theoretical and Experimental Studies of Zero-G Heat Transfer Modes, Monthly Progress Report for the Period 27 March 1966 to 1 May 1966, Contract NAS 8-11525, Sunnyvale, Calif., 16 May 1966

4. -----, Theoretical and Experimental Studies of Zero-G Heat Transfer Modes, Monthly Progress Report for the Period 1 November 1964 to 29 November 1964, Contract NAS 8-11525, Sunnyvale, Calif., 4 Dec 1964

5. -----, Theoretical and Experimental Studies of Zero-G Heat Transfer Modes, Monthly Progress Report for the Period 31 October 1965 to 28 November 1965, Contract NAS 8-11525, Sunnyvale, Calif., 6 Aug 1965

6. L. S. Tong, Boiling Heat Transfer and Two-Phase Flow, New York, John Wiley & Sons, 1965

7. Lockheed Missiles & Space Co., RIFT Cryogenics Fluid Flow, 40-Inch Tank Gross Flow Tests, Final Report, NSP-63-70, 12 Jun 1963

8. -----, Liquid Hydrogen Stratification Data Analysis, 40-Inch Diameter Tank Gross Flow Tests, by F. L. Hines, LMSC A304894, 21 Nov 1965

9. Martin Company, Analytical and Experimental Determination of Liquid Hydrogen Temperature Stratification, Final Report, NASA-CR-63-5, Apr 1963

10. Lockheed Missiles & Space Company, Theoretical and Experimental Studies of Zero-G Heat Transfer Modes, Monthly Progress Report for the Period 29 May 1966 to 26 Jun 1966, Contract NAS 8-11525, Sunnyvale, Calif., 11 Jul 1966

LOCKHEED MISSILES & SPACE COMPANY

11. Lockheed Missiles & Space Company, <u>Theoretical and Experimental Studies of Zero-G Heat Transfer Modes,</u> Monthly Progress Report for the Period 30 May 1965 to 27 Jun 1965, Contract NAS 8-11525, Sunnyvale, Calif., 7 Jul 1965

12. Abromovich, G. N., <u>The Theory of Turbulent Jets,</u> M.I.T. Press, 1963, pp. 475-489

13. Stanford University, Department of Mechanical Engineering, <u>Use of Hydrogen Bubbles for Quantitative Determination of Time-Dependent Velocity Fields in Low-Speed Water Flows,</u> by F. A. Schraub, S. J. Kline, J. Henry, P. W. Runstadler, Jr., and A. Littell, Report MD-10

14. -----, <u>Capillary Hydrostatics and Hydrodynamics at Low-G,</u> by W. C. Reynolds, M. A. Saad, and H. M. Satterlee, TR-L6-3, Sep 1964

15. Swalley, F. E., Platt, G. K., Hastings, L. J., "Saturn V Low Gravity Fluid Mechanics Problems," Paper 1, <u>Proceedings, Symposium on Fluid Mechanics and Heat Transfer Under Low Gravity,</u> Jun 1965, Palo Alto, Calif.

16. Shanks, E. B., <u>Higher Order Approximations of Runge-Kutta Type,</u> NASA-TN-D-2920, Sep 1965

Appendix

MENSLM COMPUTER PROGRAM

SUMMARY

MENSLM (Meniscus Shape with Liquid Motion) is a computer program written in
FORTRAN IV for calculating the meniscus shape of a liquid in a cylindrical container,
taking into account the effects of fluid motion. The program involves numerical in-
tegrations, using a fourth-order Runge-Kutta scheme, of a nonlinear ordinary differ-
ential equation of second order with two-point boundary conditions. Details of the
program, including input-output formats, are described in this Appendix.

DESCRIPTION OF NUMERICAL METHODS

The differential equation and boundary conditions for the free surface of a liquid in a
cylindrical container have been given in Eq. (2.9) of Ref. 1. The equation is

$$\frac{1}{r}\frac{d}{dr}\left[\frac{rF_r}{\left(1 + F_r^2\right)^{1/2}}\right] - 2\,F_{rr}\,(0) - BoF - \frac{We}{2}U^2 = 0 \tag{1}$$

and the boundary conditions are

$$F_r\,(0) = 0 \tag{2}$$

$$F_r\,(1) = \cot\theta \tag{3}$$

where

F   =   liquid height above datum at $r = 0$ normalized by container radius;
hence $F(0) = 0$

A-1

r = radial distance normalized by container radius

Bo = $g R^2 \rho/\sigma$, Bond number (Denoted as B in program language)

We = $u_s^2 R \rho/\sigma$, Weber number based on maximum surface velocity u_s and container radius R . (Denoted as W in program language)

U = local velocity divided by the maximum surface velocity. (Denoted as V in program language)

θ = contact angle at container wall

ρ = liquid density

σ = liquid surface tension

g = acceleration

Because of the two-point boundary conditions, the numerical solution requires iterations by assuming $F_{rr}(0)$, integrations to r = 1 , and checking θ . For a given Bond number and velocity distribution, there exists a limiting Weber number above which numerical solutions cannot be obtained within the numerical model used. This limiting Weber number is obtained by numerical iterations.

Numerical integration of Eq. (1) is performed using the common Runge-Kutta fourth-order formula (Ref. 16) with a uniform input integration step size. One nonlinear characteristic of Eq. (1) is that F_r may change from a small number to a very large number in one integration step, if the assumed $F_{rr}(0)$ is not near the correct value. To prevent computer overflow, the values of the change of F_r and F are checked at each of the four Runge-Kutta integration steps. The integration process is stopped when these values exceed a large number and the iteration cycle is continued with a more appropriate value of $F_{rr}(0)$.

A-2

Let

$$\text{FPRIM}\left[F_r, \, We, \, U, \, Bo, \, F, \, F_{rr}(0), \, \frac{F_r}{r\left(1 + F_r^2\right)^{1/2}}\right]$$

$$= \left(1 + F_r^2\right)^{3/2}\left[We \frac{U^2}{2} + BoF + 2 \, F_{rr}(0) - \frac{F_r}{r\left(1 + F_r^2\right)^{1/2}}\right] \qquad (4)$$

Then, Eq. (1) may be written as

$$\frac{dF_r}{d_r} = \text{FPRIM}\left[F_r, \, We, \, U, \, Bo, \, F, \, F_{rr}(0), \, \frac{F_r}{r\left(1 + F_r^2\right)^{1/2}}\right] \qquad (5)$$

$$\frac{dF}{dr} = F_r \qquad (6)$$

Let

$$H = r_{n+1} - r_n, \text{ integration step size} \qquad (7)$$

$$F\,K1 = H \, \cdot \, F_r\,(r_n) \qquad (8)$$

$$\text{FKP1} = H \, \cdot \, \text{FPRIM}\left\{F_r\,(r_n), \, We, \, U\,(r_n), \, Bo, \, F\,(r_n), \, F_{rr}(0), \right.$$

$$\left. \frac{F_r\,(r_n)}{r_n\left[1 + F_r^2\,(r_n)\right]^{1/2}}\right\} \qquad (9)$$

A-3

$$FK2 = H \cdot \left[F_r (r_n) + \frac{FKP1}{2} \right] \tag{10}$$

$$FKP2 = H \cdot FPRIM \left\{ \left[F_r (r_n) + \frac{FKP1}{2} \right], We, U\left(r_n + \frac{H}{2}\right), Bo, \right.$$

$$\left. \left[F(r_n) + \frac{FK1}{2} \right], F_{rr}(0), \frac{\left[F_r(r_n) + \frac{FKP1}{2} \right]}{\left(r_n + \frac{H}{2}\right)\left\{ 1 + \left[F_r(r_n) + \frac{FKP1}{2} \right]^2 \right\}^{1/2}} \right\} \tag{11}$$

$$FK3 = H \cdot \left[F_r (r_n) + \frac{FKP2}{2} \right] \tag{12}$$

$$FKP3 = H \cdot FPRIM \left\{ \left[F_r (r_n) + \frac{FKP2}{2} \right], We, U\left(r_n + \frac{H}{2}\right), Bo, \right.$$

$$\left. \left[F(r_n) + \frac{FK2}{2} \right], F_{rr}(0), \frac{\left[F_r(r_n) + \frac{FKP2}{2} \right]}{\left(r_n + \frac{H}{2}\right)\left\{ 1 + \left[F_r(r_n) + \frac{FKP2}{2} \right]^2 \right\}^{1/2}} \right\} \tag{13}$$

$$FK4 = H \cdot \left[F_r (r_n) + FKP3 \right] \tag{14}$$

$$FKP4 = H \cdot FPRIM \left\{ \left[F_r (r_n) + FKP3 \right], We, U(r_n + H), B_o, \right.$$

$$\left. \left[F(r_n) + FK3 \right], F_{rr}(0), \frac{\left[F_r(r_n) + FKP3 \right]}{\left(r_n + H\right)\left\{ 1 + \left[F_r(r_n) + FKP3 \right]^2 \right\}^{1/2}} \right\} \tag{15}$$

$$FFK = FK1, FKP1, FK2, FKP2, FK3, FKP3, FK4, FKP4 \text{ consecutively}$$

Then, whenever

$$|FFK| \geq 10^7 \tag{16}$$

the integration process is stopped and the iteration cycle is continued with a more appropriate value of $F_{rr}(0)$. If $|FKP4| < 10^7$, the integration is advanced to the next step with

$$F(r_{n+1}) = F(r_n) + (FK1 + 2 \cdot FK2 + 2 \cdot FK3 + FK4)/6 \tag{17}$$

$$F_r(r_{n+1}) = F_r(r_n) + (FKP1 + 2 \cdot FKP2 + 2 \cdot FKP3 + FKP4)/6 \tag{18}$$

Then, if $|F_r(r_{n+1})| \geq 10^5$, the integration is again stopped and the iteration cycle is continued with a new value of $F_{rr}(0)$. If $|F_r(r_{n+1})| < 10^5$, the integration is continued. The above process is repeated until the wall, $r = 1$, is reached. If the contact-angle boundary condition is not satisfied, the iteration process is continued with a new value of $F_{rr}(0)$. The iteration method for obtaining a correct value of $F_{rr}(0) = FRR$ is described schematically in Fig. A-1. New lower-bound or upper-bound values of FRR are calculated whenever the conditions $|FFK| - 10^7 < 0$, $|F_r| - 10^5 < 0$, or $|\theta' - \theta| - \delta\theta \leq 0$ are not satisfied. The value of contact-angle accuracy $\delta\theta$ and the FRR step size (denoted as DELTA and DELFR in machine language) are input. Typical values used are DELTA = 0.5 deg and DELFR = 1.0. The value of ZFRR used is 2.0×10^{-8} (see next paragraph). The input is shown in Fig. A-2.

Observation of the numerical values of $F_{rr}(0)$, as the iteration progresses, indicates that only a very small change of $F_{rr}(0)$ values is necessary to go from no solution to a solution. Therefore, the following criterion for defining the limiting Weber number is selected. Let

$$ZFRR \equiv \zeta \equiv \left| \frac{F_{rr}(0)_n - F_{rr}(0)_{n+1}}{F_{rr}(0)_{n+1}} \right| \tag{19}$$

A-5

Fig. A-1 FRR Iteration Schematic

Weber Number Iteration, Fig. A-3

D   C

Check $\left|\dfrac{FRR1-FRR}{FRR}\right| - ZFRR$

set upper FRR   set lower FRR

| FH = FRR
FRR1 = FRR
JFLAG = −1
FRR = FRR −
(FH−FL)/2 | FH = FRR
FRR1 = FRR
LL = 1
FRR = FRR − δF | FL = FRR
FRR1 = FRR
LL = 1
FRR = FRR + δF | FL = FRR
FRR1 = FRR
JFLAG =−1
FRR = FRR +
(FH − FL)/2 |

Check LL   Check LL

Check JFLAG   Check FFK   Check JFLAG

B

Check F_r

Solutions and Weber Number Iteration, Fig. A-3

Check $|\theta' - \theta| - \delta\theta$ E

Check $\theta' - \theta$

A   B

$\theta' = \tan^{-1}\left(\dfrac{1}{-F_r}\right)$ $\theta' = \dfrac{\pi}{2}$ $\theta' = \pi - \tan^{-1}\left(\dfrac{1}{-F_r}\right)$

Check F_r

Check $r - 0.99999$ Check $|F_r| - 10^5$ Check $|FFK| - 10^7$ Initial B.C.
$r = 0$
$F = 0$
$F_r = 0$ Begin
JFLAG = 0
LL = 0
FRR2 = FRR

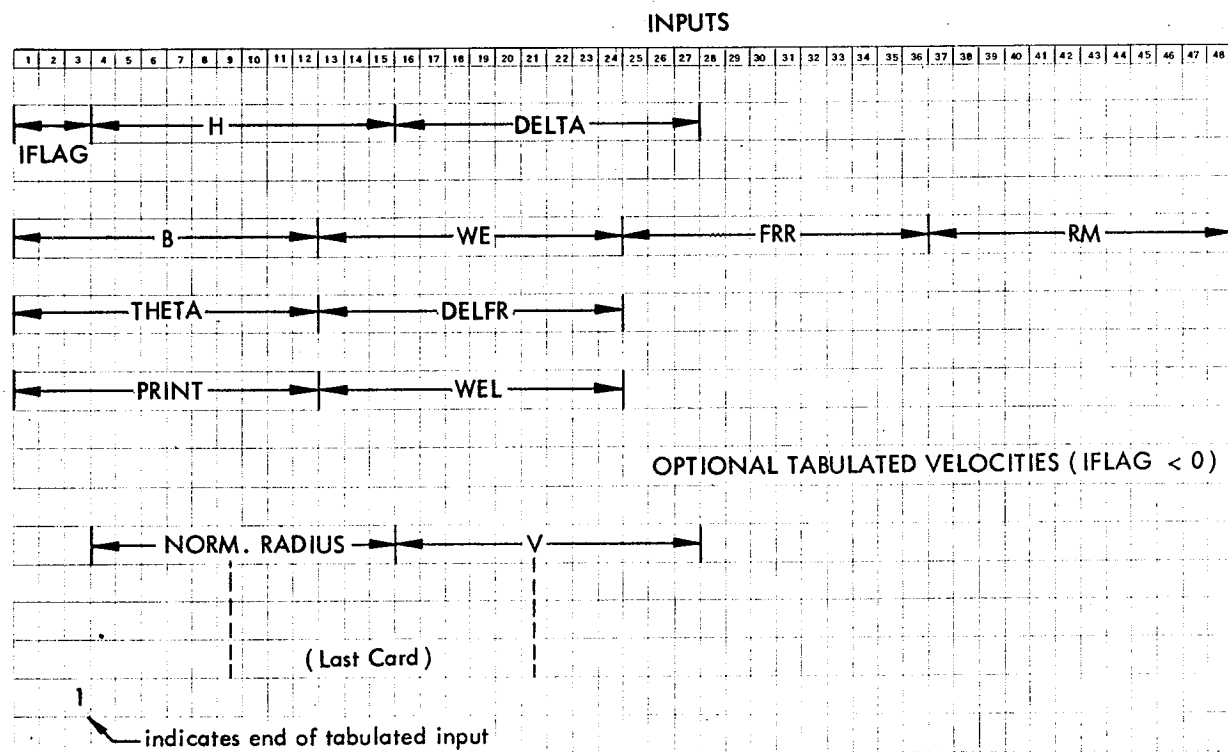Runge-Kutta steps

Continue integration

C

A

Fig. A-2 Computer Input

where n and $n + 1$ are numbers of iterations. If $\zeta > 2 \times 10^{-8}$, iteration with respect to $F_{rr}(0)$ continues with the input Weber numbers. Further iterations with respect to $F_{rr}(0)$ will eventually either yield a valid solution for the input Weber number or make $\zeta \leq 2 \times 10^{-8}$. If $\zeta \leq 2 \times 10^{-8}$, the Weber number input is greater than the limiting value. The next iteration then begins with a lower value of We given by

$$We_{n+1} = (We_n + WL_n)/2 \tag{20}$$

where WL_n is a lower-bound We at the nth iteration. A new upper-bound $WU_{n+1} = We_n$ is also set. If, during subsequent iterations of values of We, the lower-bound and upper-bound values differ by 5 percent or less, the limiting Weber number is considered reached. Since the surface velocity distribution is generally not accurately known, a 5-percent accuracy in the limiting Weber number should be adequate. The iteration method for obtaining a limiting $We = WE$ and the print output control are described schematically in Fig. A-3. The value of the lower-bound Weber number, WEL, and the print-control variable, $PRINT$, are input. The options for $PRINT$ are as follows:

$$PRINT \begin{cases} < 0.0 & \text{print limiting } We \text{ value only} \\ = 0.0 & \text{print surface shape for limiting } We \\ > 0.0 & \text{print surface shape for all } We \text{ values during iteration} \end{cases}$$

The current trial values of WE are also printed out during iterations.

Two options are provided in specifying the surface velocity distributions. One option employs a table input (using Subroutine $TBLP$) of values of U versus r. The second option (using subroutine $GFUN$) involves the use of analytic velocity distribution functions. The function considered first during this study was the "double-sine" velocity

A-8

Check $\left|\dfrac{FRR1-FRR}{FRR}\right| - ZFRR$

© C > 0. Fig. A-1

Ⓓ ≤ 0

WEU−WE

Check WEU ≤ 0 → Model not adequate, next case

> 0

Check $\dfrac{WEU-WEL}{WEU} - 0.05$ ≤ 0 → Limiting W Within 5%

> 0

$WE = \dfrac{WEU + WEL}{2}$

Limiting W Within 5% → Check PRINT ≠ 0 → Next Case

= 0

WE = WEL
FRR2 = FRR3

JFLAG = 0
LL ≠ 0
FRR = FRR2

Next Trial W

© C Fig. A-1

WEL = WE
FRR3 = FRR ≤ 0 Check PRINT

WX = 1 Solution FRR > 0

Check WX > 0 ... ≤ 0 → Next Case

Print Surface Shape

Check $\left|\theta'-\theta\right| - \delta\theta$ > 0 Fig. A-1

Ⓔ ≤ 0

Check WE ≤ 0 → WX = 0

> 0

Check $\dfrac{WEU-WE}{WEU} - 0.05$ ≤ 0 → WX = 0

> 0

Check WEU − WE ≤ 0 → Print Surface Shape

> 0

Check PRINT ≥ 0

< 0 → Limiting W Within 5%, Next Case

Fig. A-3 Weber Number Iteration and Print Control Schematic

distribution given by the following expressions:

$$U = \begin{cases} \sin(r/r_m) & , \quad 0 \leq r \leq r_m \\ \sin\left(\dfrac{1-r}{1-r_m}\right) & , \quad r > r_m \end{cases} \tag{21}$$

where r_m is the value of r at $U = 1$, corresponding to $u = u_s$. However, any one-parameter distribution function may be used in place of Eq. (21) in the second option. A sample of the output format is shown in Fig. A-4.

A-10

NEXT CASE

| WEBER NUMBER | .100000+04 | BOND NUMBER | .100000+02 | CONTACT ANGLE | .500000+01 |

ANALYTIC VELOCITY DISTRIBUTION

WE= .10000000+04 TOO LARGE, WEL= .00000000 FRR1= -.11457285+02 FRR= -.11457285+02

NEXT TRIAL WE = .50000000+03

WE= .50000000+03 TOO LARGE, WEL= .00000000 FRR1= -.76118433+01 FRR= -.76118432+01

NEXT TRIAL WE = .25000000+03

WE= .25000000+03 TOO LARGE, WEL= .00000000 FRR1= -.48117181+01 FRR= -.48117180+01

NEXT TRIAL WE = .12500000+03

WE= .12500000+03 TOO LARGE, WEL= .00000000 FRR1= -.30079047+01 FRR= -.30079047+01

NEXT TRIAL WE = .62500000+02

WE= .62500000+02 TOO LARGE, WEL= .00000000 FRR1= -.15509483+01 FRR= -.15509484+01

NEXT TRIAL WE = .31250000+02
     YIELDS SOLUTION WITH FRR= -.62512207-00

NEXT TRIAL WE = .46875000+02
     YIELDS SOLUTION WITH FRR= -.10964813+01

NEXT TRIAL WE = .54687500+02
     YIELDS SOLUTION WITH FRR= -.13267412+01

NEXT TRIAL WE = .58593750+02

WE= .58593750+02 TOO LARGE, WEL= .54687500+02 FRR1= -.14397453+01 FRR= -.14397454+01

NEXT TRIAL WE = .56640625+02

F DOUBLE PRIME AT R = 0   -.13834558+01

R	F	FPRIME
.000000	.000000	.000000
.500000-01	-.170471-02	-.664479-01
.100000+00	-.648361-02	-.122772+00
.150000-00	-.138213-01	-.169330-00
.200000-00	-.233091-01	-.209346-00
.250000-00	-.346963-01	-.245702-00
.300000-00	-.478482-01	-.280122-00
.350000-00	-.626855-01	-.313099-00
.400000-00	-.791233-01	-.343924-00
.450000-00	-.970103-01	-.370617-00
.500000-00	-.116060+00	-.389720-00
.550000-00	-.135771-00	-.396036-00
.600000-00	-.155336-00	-.382539-00
.650000-00	-.173555-00	-.340753-00
.700000-00	-.188789-00	-.261554-00
.750000-00	-.198929-00	-.135179-00
.800000-00	-.201289-00	.532607-01
.850000-00	-.191964-00	.343736-00
.900000-00	-.162814-00	.906247-00
.950000-00	-.776529-01	.374094+01
.100000+01	.846323-00	.114142+02

Fig. A-4 Sample Output Format

A-11